Chapter 2

Numerical modelling and simulation

This chapter covers the numerical simulation set-up. Background is given about the material model that was used. The different parameters of the material model are discussed. A validation test was conducted to ensure that the numerical simulation performs as expected. Finally the model set-up is investigated to show the influence of the different model parameters. The information gathered in this chapter was used to determine the model parameters for the final set-up of the numerical simulations.

2.1 The continuous surface cap model theory

The continuous surface cap model (CSCM) is one of many concrete material models available in LS-DYNA and is discussed in section 1.4.10. LS-DYNA is an explicit finite element code found in ANSYS. The material model must be coded into ANSYS in a keyword format as either `MAT_CSCM` or `MAT_CSCM_CONCRETE`. The CSCM was developed to simulate failure and deformation of concrete used for the National Cooperative Highway Research Program (NCHRP) 350 roadside safety hardware testing. The project was funded by the Federal Highway Administration (Jaime et al., 2015). Currently the available rock failure models are all for concrete as discussed in section 1.4.10. Thus the parameters for the model must be changed to model other rock types. The material model includes the following features, elasticity, plasticity, hardening, damage, and rate effects. The main purpose of the material model are to model strain softening in the tensile and low confining pressure regimes.

Concrete exhibits complex behaviour depending on the confining pressure. The CSCM assumes that concrete has isotropic elastic behaviour before cracks initiate. It assumes that concrete has a low tensile strength. The model assumes that the unconfined tension strength is between eight to fifteen percent of the unconfined compression strength. In tensile and low confining pressure regimes concrete softens to nearly zero strength whereas at moderate pressures, the concrete will exhibit residual strength as it softens. The stiffness of concrete degrades as softening occurs. The model takes into account strain rate, which has an effect on the strength of the concrete. As the strain rate increases, the strength also increases.

The CSCM has six formulations namely, elastic update, plastic update, yield surface definition, damage, rate effects, and kinematic hardening. Hooke's law is used for the elastic stress-strain relationship it takes into account the bulk modulus and the shear modulus. Both material properties are required. Like most materials, concrete has an initial elastic phase whereafter it will yield and failure will occur. The CSCM has a three-dimensional yield surface as shown in figure 2.1. A plasticity algorithm sets the initial yield stresses.

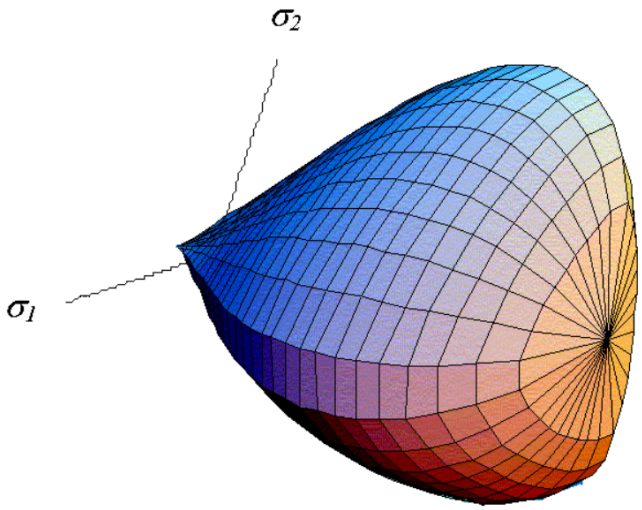

Figure 2.1: General shape of the concrete model yield surface in three dimensions (Trentacoste, 2007).

An incremental form of Hooke's law is used to update the stress at each time step. This updated stress is called the trail elastic stress. After the trail elastic stress is determined, its position is checked. If the trail elastic stress lies either inside or on the yield surface the behaviour is elastic. When the behaviour is elastic the plasticity algorithm is bypassed. But if the trail elastic stress lies outside the yield surface, the behaviour is elastic-plastic. When the behaviour is elastic-plastic the plasticity algorithm is used to return the stress state to the yield surface. The new stress state is called the inviscid stress. When the behaviour is elastic-plastic there is a possibility for hardening, damage and rate effect. The algorithm enforces the plastic consistency condition with associated flow. To ensure accuracy and efficiency, subincrementation is utilized instead of iteration when returning the stress state to the yield surface.

The CSCM consists of a shear surface and a hardening cap as can be seen in figure 2.2. There is a smooth continuous interaction between the shear surface and cap to reduce the numerical complexity. The CSCM model has three independent stress invariants. All three of the stress invariants are used to formulate the yield surface. The CSCM model uses the first invariant of the stress tensor and the second and third invariant of the deviatoric stress tensor. The deviatoric stress tensor and pressure is used to establish the invariants. The yield surface formulation also takes a hardening parameter into account.

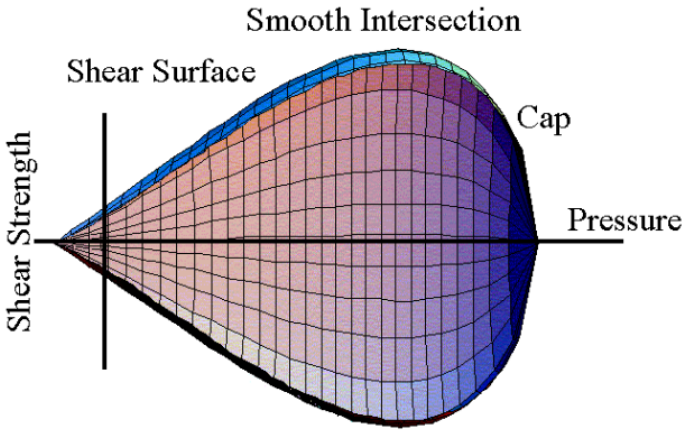

Figure 2.2: General shape of the concrete model yield surface in two dimensions in the meridonal plane (Trentacoste, 2007).

The yield surface consists out of three sections, tensile, low confining pressure regimes and moderate to high confining pressure regimes as shown in figure 2.3.

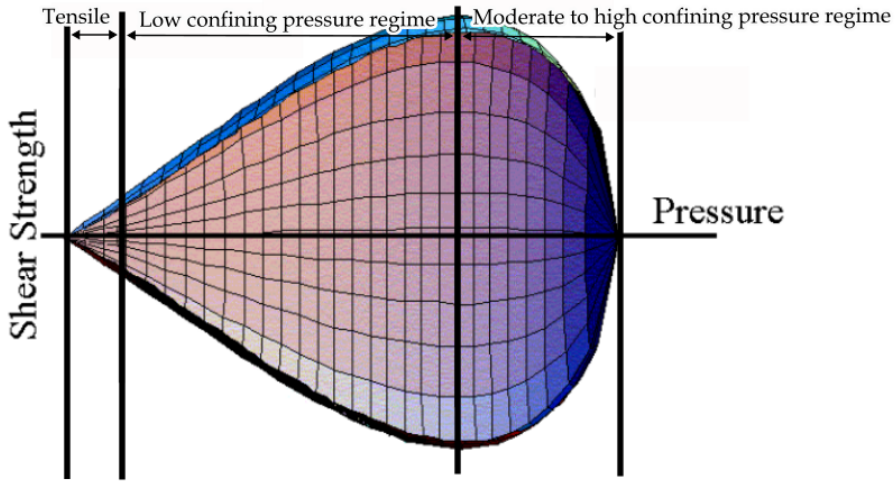

Figure 2.3: Sections of yield surface in two dimensions in the meridonal plane. Adapted from (Trentacoste, 2007)

In the tensile and low confining pressure regimes the yield surface is modelled by a shear surface and in the moderate to high confining pressure regimes, the yield surface is modelled by a hardening cap. In the compression meridian the shear surface is defined by equation 2.1,

$$F_f(I_1) = \alpha - \lambda \exp^{-\beta I_1} + \theta I_1 \tag{2.1}$$

where α, β, λ and θ are parameters that are optimized by fitting the strength measurements from a triaxial compression test, conducted on a plain cylinder, to the model surface. Figure 2.4 shows the compressive shear surface. The data is plotted as principal stress difference versus pressure.

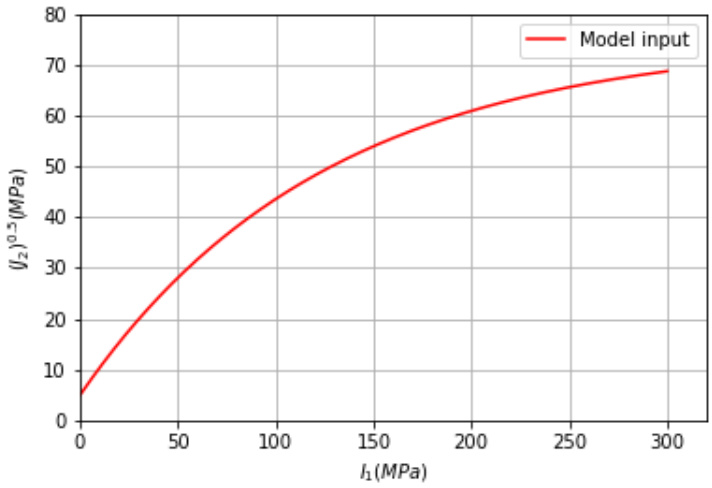

Figure 2.4: Compressive shear surface

In the moderate to high confining pressure regime the cap is used to model plastic volume change due to pore collapse. But the CSCM does not explicitly model the pores. The onset of plasticity in isotropic compression and uniaxial strain is determined by the cap's initial position. The cap's elliptical shape results in a greater onset for isotropic compression compared to uniaxial strain, which is consistent with data on shear enhanced compaction. The cap is made to move, expanding and contracting, in accordance with the hardening rule to simulate plastic volume change. The hardening rule is a built in equation in the LS-DYNA software. Equation 2.2 shows the hardening rule,

$$\varepsilon_V^p = W\left(1 - \exp^{-D_1(X-X0)-D_2(X-X_0)^2}\right) \tag{2.2}$$

where ε_V^p is the plastic volume strain and W, D_1, D_2 and X_0 are user defined parameters. W is the maximum plastic volume strain and X_0 is the initial location of the cap. The isotropic compression curve is used for the parameter calibration. Figure 2.5 shows an example of an isotropic compression curve.

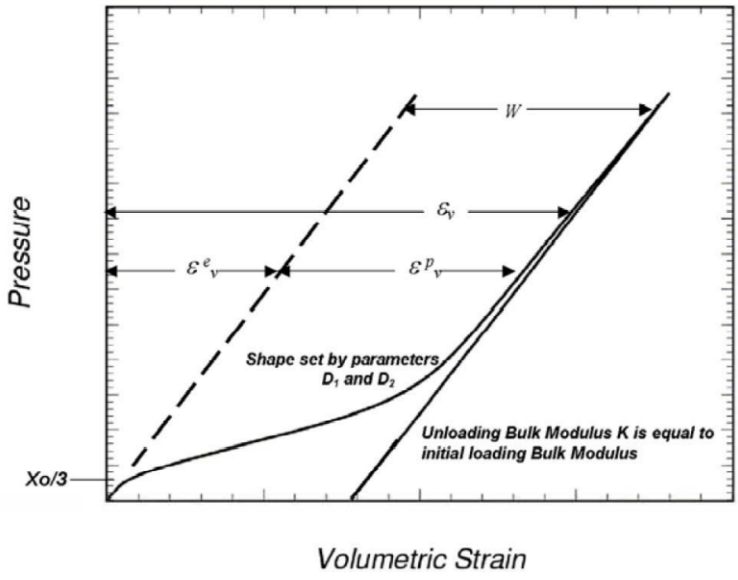

Figure 2.5: Example of an isotropic compression curve (Jaime, 2011)

To determine the parameters, the pressure-volumetric strain curve in isotropic compression is used. X_0 is the initial cap location. The initial cap location is the pressure invariant where compaction initiates in isotropic compression. This location is where the isotropic compression curve becomes non-linear, this can be the intercept of the curve if the curve is non-linear throughout.

W is the range over which the pressure-volumetric strain is non-linear, measured in volumetric strain. After W and X_0 is determined D_1 and D_2 is determined by fitting equation 2.2 to the isotropic compression curve. Figure 2.6 shows the isotropic compression curve for equation 2.2.

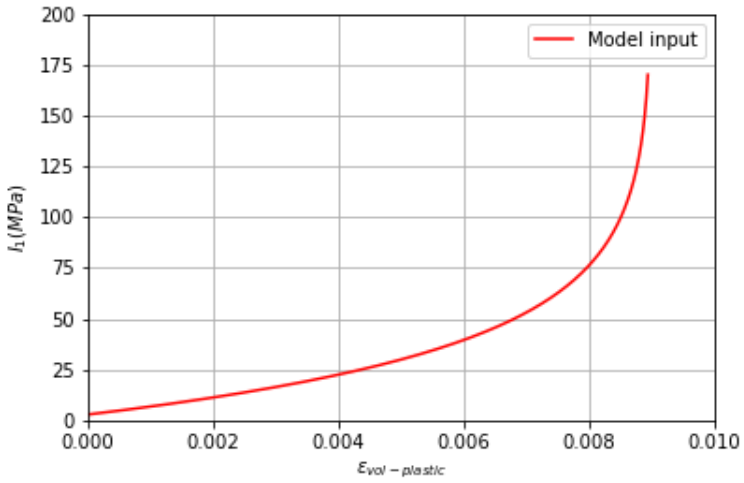

Figure 2.6: Isotropic compression curve for equation 2.2

The strength of concrete relative to triaxial compression (TXC) for any state of stress is determined by the Rubin scaling function. Simulating strengths such as triaxial extension (TXE) and triaxial shear (TOR) is achieved by scaling back the TXC shear strength using the Rubin scaling function. The Rubin function is a scaling function that alters the yield surface's shape in the deviatoric plane based on the angle $\hat{\beta}$, as demonstrated in figure 2.7.

The CSCM uses the Rubin three-invariant formulation because it is more flexible in fitting data. There are two Rubin scaling functions used in the calibration process. One for the triaxial shear test and one for the triaxial extension test namely, Q_1 and Q_2. There are four different methods of fitting the Rubin formulation. The most common fit is given by equations 2.3 and 2.4 where equation 2.3 shows the equation of the shear surface along the tensile meridian,

$$Q_2 = \alpha_2 - \lambda_2 \exp^{-\beta_2 J_1} + \theta_2 J_1 \tag{2.3}$$

where α_2, β_2, λ_2 and θ_2 are parameters that are optimized by fitting the strength measurements from the triaxial extension test, that was conducted on a plain cylinder, to the model surface. Equation 2.4 shows the equation of the shear surface along the shear meridian,

$$Q_1 = \alpha_1 - \lambda_1 \exp^{-\beta_1 J_1} + \theta_1 J_1 \tag{2.4}$$

where α_1, β_1, λ_1 and θ_1 are parameters that are optimized by fitting the strength measurements from the triaxial shear test, that was conducted on a plain cylinder, to the model surface.

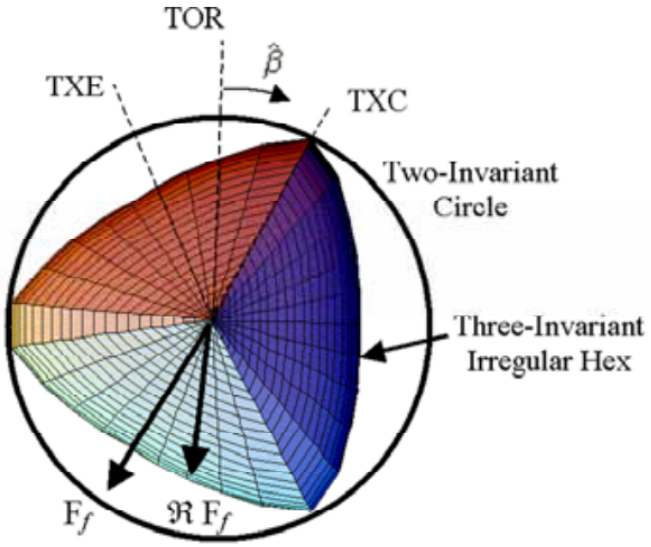

Figure 2.7: Example two- and three-invariant shapes of the concrete model in the deviatoric plane (Trentacoste, 2007).

At present, the shape of the three-invariant yield surface is determined by the eight input parameters defining Q_1 and Q_2 only under compressive pressure, not tensile pressure. Under tensile pressure, the model sets Q_1 = 0.5774 and Q_2 = 0.5, generating a triangular yield surface in the deviatoric plane that cannot be overridden. This yields approximately equal strengths in uniaxial, equal biaxial, and equal triaxial tensile stress simulations. To ensure a smooth transition between the tensile and compressive pressure regions, the user must set Q_1 = 0.5774 and Q_2 = 0.5 at zero pressure by setting $\alpha_1 - \lambda_1 = 0.5774$ and $\alpha_1 - \lambda_1 = 0.5774$.

The CSCM models softens only in the tensile and low confining pressure regimes. In the damage formulation, both strain softening and modulus reduction are modeled. Strain softening refers to a reduction in strength after reaching the peak strength value during progressive straining. Modulus reduction refers to a decrease in the slope of unloading/loading observed during cyclic unload/load tests.

The damage parameter is used to change the stress tensor without damage to a stress tensor with damage. The damage parameter ranges between zero, which states no damage, and one, which states complete damage. The damage is introduced by multiplying the stress tensor without damage with, the value obtained of one minus the damage parameter. The damage is introduced after the update of the viscoplasticity algorithm. The initiation and accumulation of damage occur when the strain-based energy terms surpass the damage threshold. Damage accumulation, quantified by the damage parameter, is based on two distinct formulations, namely brittle damage and ductile damage.

Brittle damage only accumulate when the pressure is tensile, whereas ductile damage only accumulate when the pressure is compressive. The accumulation of brittle damage is dependent on the maximum principal strain whereas the accumulation of ductile damage is dependent on the total strain component. Plasticity triggers both brittle and ductile damage initiation. This implies that the initial damage surface is aligned with the plastic shear surface, so no separate damage surface is required to be specified by the user. Damage initiates at the peak strength of the shear surface where the plastic volume strain is dilative, whereas it does not initiate on the cap, where plastic volume strain is compactive.

Damage accumulation occurs when either the brittle or ductile energy term surpasses the current damage threshold. Following damage initiation, the damage threshold value increases. If the threshold value does not exceed the previous threshold, the threshold remains unchanged. Therefore, each threshold term, brittle or ductile, must surpass its previous maximum value for damage accumulation to occur.

For the damage accumulation three parameters must be determined. These parameters are used to determine the thresholds for ductile and brittle damage. Equations 2.5 and 2.6 show how the damage parameter, D, increases for ductile and brittle damage accumulation. To prevent excessive damage accumulation within a single time step and avoid unstable behaviour, the maximum increment in damage that can accumulate is set to 0.1.

$$D(\tau_c) = \frac{0.999}{b}\left(\frac{1+b}{1+b\exp^{-a(\tau_c-\tau_{c0})}} - 1\right) \tag{2.5}$$

$$D(\tau_t) = \frac{D_{max}}{d}\left(\frac{1+d}{1+d\exp^{-c(\tau_c-\tau_{c0})}} - 1\right) \tag{2.6}$$

The user must only specify b and d. The other parameters are internally calculated by the CSCM. a can be determined by using equation 2.7.

$$a' = a(D_{max} + 0.001)^{p_{mod}} \tag{2.7}$$

Jaime (2011) suggests a value of zero for p_{mod}. b and d are just user chosen parameters. As b increases less damage is accumulated. Thus as b increases a larger maximum compressive strength is attained.

The CSCM regulates mesh size sensitivity when softening is applied. This is done by maintaining constant fracture energy regardless of element size. There are five parameters that are used to regulate mesh size sensitivities. Three are the fracture energy values and the other two are parameters used for interpolation. The three fracture energy values are the fracture energy in uniaxial compression, G_{fc}, the fracture energy in uniaxial tension, G_{ft}, and the fracture energy in pure shear, G_{fs}. The fracture energy is the area under the stress-strain curve from zero to peak strength.

The CSCM internally calculates the fracture energy either in compression or in tension by interpolating between the three fracture energy values. The interpolation depends on the shear-to-compression transition parameter, *pwrc*, and the shear-to-tension transition parameter, *pwrt*.

Equations 2.8 and 2.10 show the interpolation equations for compression and tension. Equations 2.9 and 2.11 shows the transition parameters used in the interpolation equations for compression and tension.

$$G_f = G_{fs} + (G_{fc} - G_{fs})trans \tag{2.8}$$

where

$$trans = \left(\frac{I_1}{\sqrt{3J_2}} \right)^{pwrc} \tag{2.9}$$

$$G_f = G_{fs} + (G_{ft} - G_{fs})trans \tag{2.10}$$

where

$$trans = \left(\frac{-I_1}{\sqrt{3J_2}} \right)^{pwrt} \tag{2.11}$$

The shear-to-compression transition parameter, *pwrc*, and the shear-to-tension transition parameter, *pwrt* must be selected by the user or by using default values.

Whenever the ductile damage formulation is active and the pressure is compressive, the ductile damage parameter increases. This occurs when the threshold exceeds the current damage threshold. The ductile damage parameter value never decreases, even temporarily.

On the other hand, the brittle damage parameter increases in value when the brittle damage formulation is active and the pressure is tensile, and the threshold exceeds the current damage threshold. When the brittle damage formulation is inactive, the damage parameter is temporarily set to zero in order to model stiffness recovery with crack closing. This means that brittle damage drops to zero, allowing stiffness to recover whenever the pressure switches from tensile to compressive. The maximum value of the damage parameter is recovered when the brittle formulation becomes active again, that is when the pressure becomes tensile once more.

A user-specified input parameter, referred to as *recov*, is available to control stiffness recovery. The default value of *recov* is zero, implying 100 percent recovery of stiffness and strength when the pressure becomes compressive. If *recov* is set to 1, there will be no recovery of stiffness and strength, resulting in brittle damage remaining at its maximum level. Values between 0 and 1 enable partial recovery to be modelled.

Lastly there are eight parameters that the user must specify for the visco-plastic rate effects. These parameters are used by internally calculated interpolation equations to add rate effects to the inviscid

stress. The interpolation is between the inviscid stress and elastic trial stress to determine the visco-plastic stress, stress with rate effects.

The interpolation is dependent on the time step and the effective fluidity coefficient. The effective fluidity coefficient is internally calculated with seven user defined parameters namely the rate effect parameter in uniaxial compression stress η_{c0}, the rate effect power in uniaxial compression stress N_c, the maximum overstress allowed in uniaxial compression stress *overc*, the rate effect parameter in uniaxial tensile stress η_{t0}, the rate effect power in uniaxial tensile stress N_t, and the maximum overstress allowed in uniaxial tensile stress *overt*. The last parameter is the effective shear stress to tensile stress fluididity parameter S_{rate}.

These parameters are determined through trial and error and initial values from Jaime (Jaime, 2011).

The final parameter is *repow* which is used to increase the fracture energy as a function of effective strain rate as seen in equation 2.12,

$$G_f^{rate} = G_f \left(1 + \frac{E\dot{\varepsilon}\eta}{f'}\right)^{repow} \tag{2.12}$$

where G_f^{rate} is the increased fracture energy due to rate effect and f' is internally calculated. The value in parenthesis will always be greater or equal to one. Thus the fracture energy will always increase independently of the positive value of *repow*. This parameter will initially be one and adjusted through trial and error.

2.2 CSCM validation

A validation test was performed on the model to ensure that the correct model set-up and parameters are used. The validation test was taken from (Huang et al., 2016) and (Su and Akcin, 2011). In (Huang et al., 2016) and (Su and Akcin, 2011) DEM results, LS-DYNA FEM results and theoretical model results from Evans (1984) are given for three different cutting depths. Su and Akein (2011) also give the dimensions of the conical pick used in the simulations. Figure 2.8 shows the parameters of the conical pick used in the simulations.

The pick used for the simulations has the following parameters (Su and Akcin, 2011). Attack angle = 57°, Tip angle = 80°, Clearance angle = 17° and Cutting depth = 3 mm, 6 mm and 9 mm.

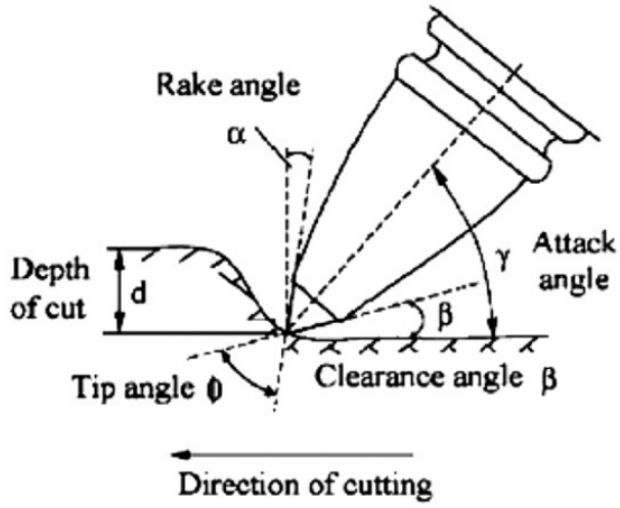

Figure 2.8: The parameters of the conical pick used in the simulations (Su and Akcin, 2011).

Figure 2.9 shows the model used for the CSCM validation, at a cutting depth of 3 mm. For the FEM simulations the two sides, bottom and back of the rock was fixed in all three directions. The cutting distance was 30 mm and the cutting speed 0.3 m/s. A sample frequency of 10 000 Hz was used. The sample frequency is used by the explicit FEM analysis to determine when the next time step is.

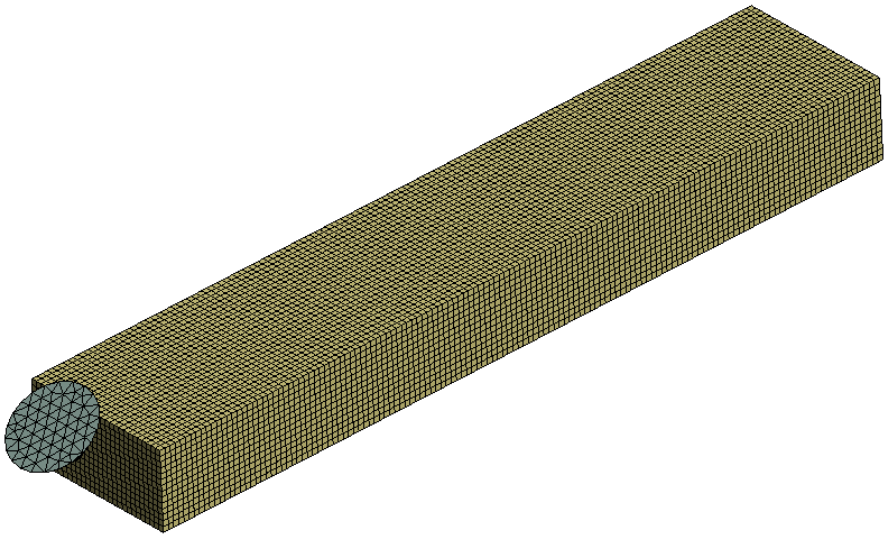

Figure 2.9: CSCM validation model, 3 mm cutting depth.

For the contact between both the pick and the rock and the rock and the rock, eroding contact was modelled with the `ERODING_SURFACE_TO_SURFACE` formulation. The contact had a viscous damping coefficient of 10, contact penalty scale factor of 10 and target penalty scale factor of 10. The formulation also allowed for interior eroding contact to occur. A friction coefficient of 0.6, a dynamic coefficient of 0.4 and a decay constant of 10 was used. These values were obtained from (Jaime, 2011) and default values. In section 2.3 the influence of these values are investigated.

For the rock, an element size of 0.25 mm was used and automatic meshing. For the pick an element size of 0.5 mm was used, but a vertex sizing with spherical influence at the tip of the pick was used with radius 1 mm and element size of 0.15 mm. The vertex sizing ensured that the element size at the tip of the pick is small. Automatic meshing was also used for the pick.

The pick is modelled as a rigid body and the rock is modelled using the CSCM. The parameters used for the CSCM is given in table 2.1. These values were determined by using equations from (Novozhilov, Dmitriev and Mikhaluk, 2022) and the rock properties given in (Su and Akcin, 2011) of the sandstone that was used in the numerical simulations. (Novozhilov, Dmitriev and Mikhaluk, 2022) requires five values, Young's modulus, Poisson's ratio, density, uniaxial compressive strength and aggregate size for the equations to determine the model parameters. Some of the model parameters were then changed through trial and error.

Table 2.1: CSCM parameters.

CSCM parameters					
Control factors			Rate effects		
ρ	2.65	g/cm^3	η_{c0}	0.002	
NPLOT	1.00		N_c	0.781	
INCRE	0.00		η_{t0}	0	
IRATE	1.00		N_t	0.48	
ERODE	1.10		*overc*	145.8433	
RECOV	10.00		*overt*	145.8433	
IRETRC	1.00		S_{rate}	1	
PRED	0.00		*repow*	1	
Shear surface hardening			Stiffness		
N_H	0.00		G_0	7100	MPa
C_H	0.00		K_0	9466.7	MPa
Damage			Yield surface		
b	100		α	58.8721	MPa
d	0.1		θ	0.266	
G_{fc}	12.0947	MPa·mm	λ	51.3169	MPa
G_{ft}	0.129	MPa·mm	β	0.0054	MPa^{-1}
G_{fs}	0.129	MPa·mm	α_1	0.82	
pwrc	5		θ_1	0	MPa^{-1}
pwrt	1		λ_1	0.2407	
pmod	0		β_1	0.0037	MPa^{-1}
			α_2	0.76	
			θ_2	0	MPa^{-1}
			λ_2	0.26	
			β_2	0.0032	MPa^{-1}
Cap Geometry and hardening					
R	1.9538				
X_0	232.0182	MPa			
W	0.0656				
D_1	0	MPa			
D_2	0	MPa^2			

The simulations were run for 3 mm, 6 mm and 9 mm cutting depth. The results are shown in table 2.2. The results show that force are in the same range of magnitude and the same range of error of

the FEM and DEM when compared to one another.

This shows that the CSCM parameters have been assigned the correct values and are a good starting point for parameter values that will be used to determine the influence of different model set-ups. Figure 2.10 also shows the von-Mises stress of the cutting proses at 20 mm for a cutting depth of 3 mm.

Table 2.2: Results of LS-DYNA simulations, FEM simulations from (Huang et al., 2016) and DEM simulations from (Su and Akcin, 2011).

d [mm]	LS-DYNA solution [kN]				FEM solution [kN]				DEM solution [kN]				Theoretical model results [kN]	
	FN	FD	FN'	FD'	FN	FD	FN'	FD'	FN	FD	FN'	FD'	FD'_{Evans}	FD'_{Goktan}
3	0.26	0.67	0.44	1.27	0.46	0.58	0.67	0.96	0.24	0.37	0.7	1.07	0.3	0.63
6	1.00	2.72	2.05	7.02	1.62	2.06	2.27	3.14	1.19	1.34	1.92	3.08	1.18	2.53
9	1.85	4.03	2.79	8.91	1.91	3.66	3.6	8	1.84	3.18	3.16	6.23	2.66	5.69

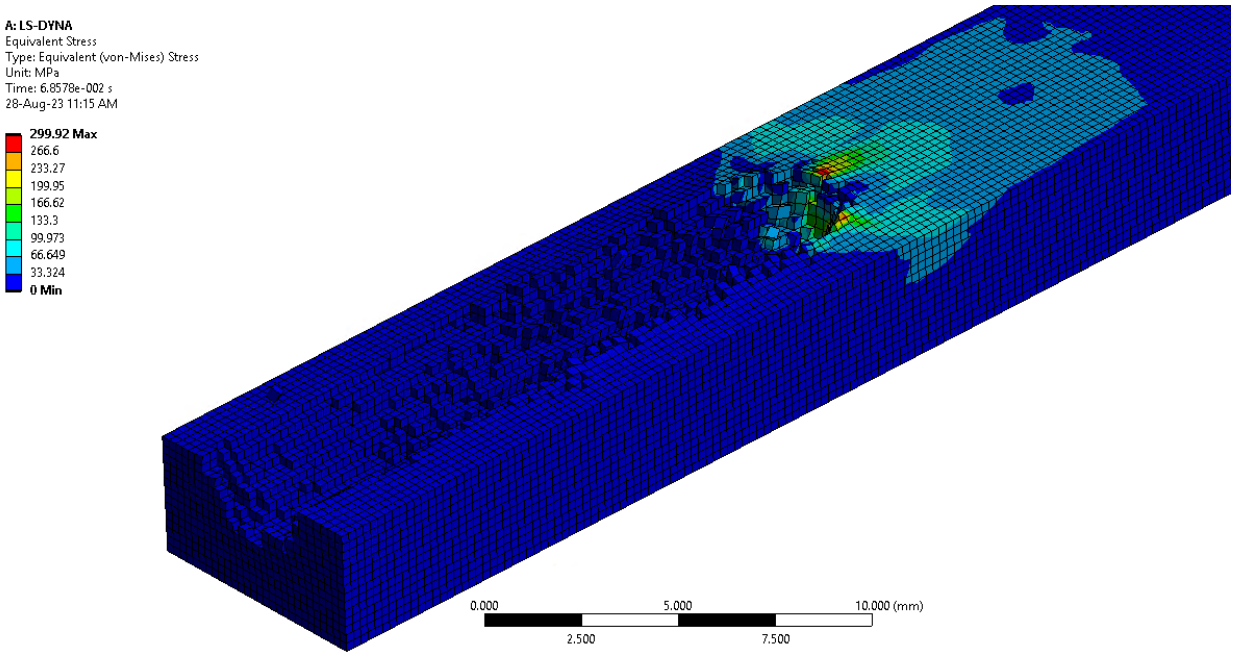

Figure 2.10: CSCM validation model, 3 mm cutting depth.

2.3 Model set-up

There are various parameters that have to be selected for the model. This includes mesh type, element size, contact properties and boundary conditions. All these parameters have an influence on the computational time, efficiency and simulation results.

The initial model used is shown in figure 2.11. Jaime (2011) recommends tetrahedron elements to be used. Tetrahedron elements allow randomness to the mesh of the rock which gives more realistic fragmentation patterns and cutting forces. The mesh type for the rock is tetrahedrons. The size of the element varies through the section. The CSCM was used for the rock with the parameters shown in

table 2.1. These parameters change throughout this section. For the FEM simulations the two sides, bottom and back of the rock were fixed in all three directions. The cutting distance was 30 mm and the cutting speed 0.3 m/s. A sample frequency of 10 000 Hz was used.

The conical pick is modelled after the conical pick that is used in the experimental laboratory scale cutting tests. The pick has an element size of 1.2 mm but a vertex sizing with spherical influence at the tip of the pick was used with radius 5 mm and element size 0.4 mm. The pick is modelled as a rigid body.
For the contact between both the pick and the rock and the rock and the rock, eroding contact was modelled with the `ERODING_SURFACE_TO_SURFACE` formulation. The contact had a viscous damping coefficient of 10, contact penalty scale factor of 10 and target penalty scale factor of 10. The formulation also allowed for interior eroding contact to occur. A friction coefficient of 0.6, a dynamic coefficient of 0.4 and a decay constant of 10 was used. These values were obtained from (Jaime, 2011) and using default values. These values will change throughout the section.

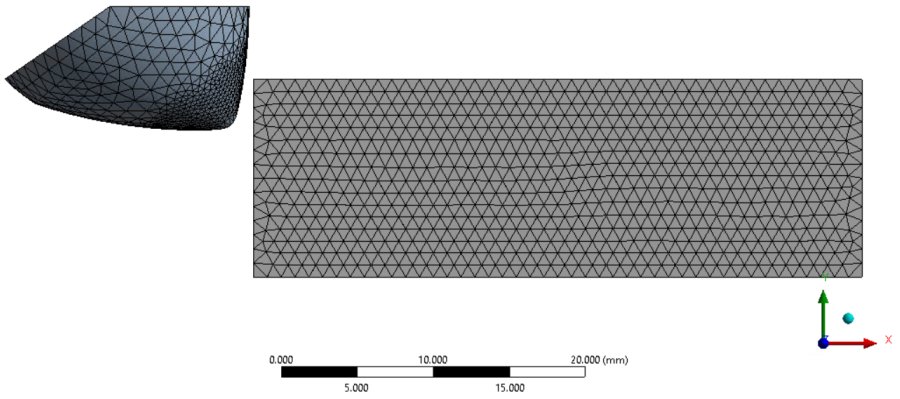

Figure 2.11: Results of three runs.

Firstly the difference in results, for the same model, is determined by running the same model three times. Due to element erosion and re-meshing, it is expected that the results will not be exactly the same for each simulation. The difference in peak forces and mean forces is investigated. Figure 2.12 shows the results of the three runs. The results are also shown in table 2.3 with the percentage error to the average value for the three runs. For the runs a cutting depth of 3 mm was used and an element size of 0.9 mm for the rock. Table 2.4 shows the ratio of the peak force to the mean force.

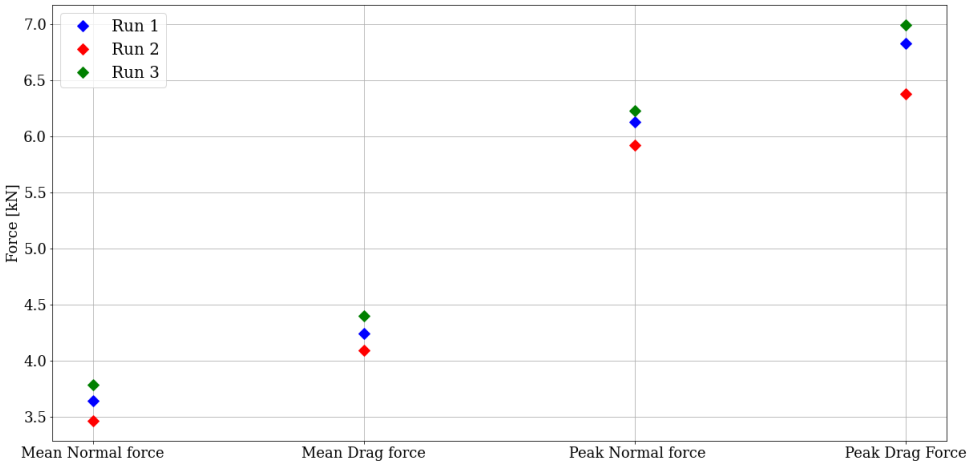

Figure 2.12: Results of three runs.

Table 2.3: Results of three runs with percentage error.

Run	FN [kN]	% Error	FD [kN]	% Error	FN' [kN]	% Error	FD' [kN]	% Error
1	3.64	0.37	4.24	0.08	6.13	0.60	6.83	1.44
2	3.46	4.60	4.09	3.61	5.92	2.84	6.38	5.25
3	3.78	4.23	4.4	3.69	6.23	2.24	6.99	3.81

Table 2.4: Results of peak to mean force ratio for three runs.

Run	Normal force ratio	Drag force ratio
1	1.68	1.61
2	1.71	1.56
3	1.65	1.59

The results of the same model run three times show an average error for the mean forces of 2.76% and an average error for the peak forces of 2.70%, but the maximum error for the peak forces are 5.24% whereas the maximum error for the mean forces are lower at 4.60%. Table 2.4 shows that the ratio of the peak force to the mean force remains relatively constant.

Owing to time constraints and the time required per run, the rest of the runs were only run once to see the influence of the change of the parameter. The results from the simulation with the changed parameters was then compared to the results of the initial parameters. This showed whether a change in parameter influenced the result of the numerical simulation.

The size of the elements determines the number of elements and the number of elements has an effect on the computational time. Different element sizes were used and the results for the mean forces and peak forces were looked at. Four different element sizes were used namely 1.4 mm, 0.9 mm, 0.6 mm and 0.4 mm. By reducing the element size it was expected that the results would converge. The ratios of the mean force to the peak force were also determined.

Figure 2.13 shows the results for the different element sizes, with a 5% error band. Table 2.5 shows how the results converge as the element size is reduced. Table 2.6 shows the peak to mean force ratio of the different element sizes.

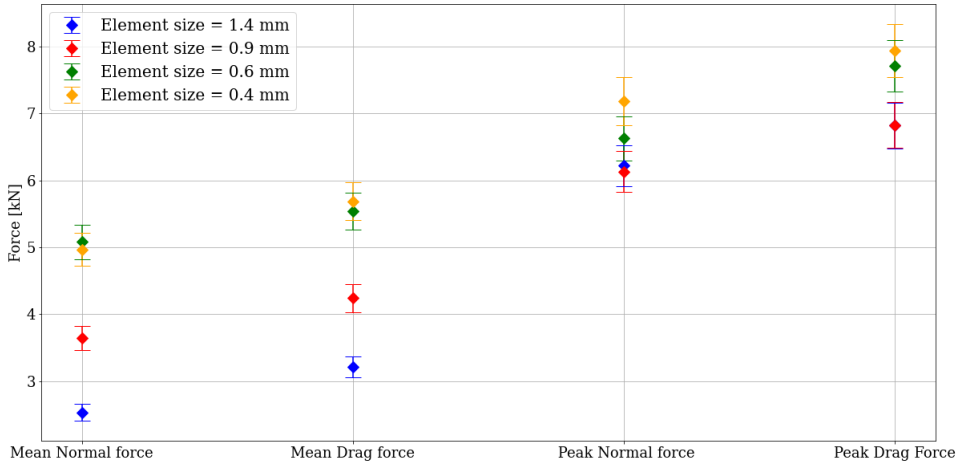

Figure 2.13: Results of different element sizes.

Table 2.5: Results of different element sizes.

Element size [mm]	FN [kN]	% Error	FD [kN]	% Error	FN' [kN]	% Error	FD' [kN]	% Error
1.4	2.53		3.21		6.22		6.82	
0.9	3.64	30.49	4.24	24.29	6.13	1.47	6.83	0.15
0.6	5.08	28.35	5.54	23.47	6.63	7.54	7.71	11.41
0.4	4.97	2.21	5.69	2.64	7.19	7.79	7.94	2.9

Table 2.6: Results of peak to mean force ratio for different element sizes.

Element size [mm]	Normal force ratio	Drag force ratio
1.4	2.46	2.12
0.9	1.68	1.61
0.6	1.31	1.39
0.4	1.45	1.4

From figure 2.13 and table 2.5, it is clear that the results converge as the element size is reduced. This is as expected. Thus, the element size and peak force to mean force ratios in table 2.6 are important to consider when deciding on element size for the final runs. The element size will be chosen by comparing the peak force to mean force ratios of the experimental results.

The boundary conditions have an influence on the force results. Three different boundary conditions were investigated. The first has both sides fixed and the back fixed, the second has only the back fixed and the third has only the sides fixed. In all three cases the bottom is fixed. For these tests the element size of the rock was 0.9 mm and the cutting depth 3 mm.

Figure 2.14 shows the results of the different boundary conditions. Table 2.7 show the results for the ratio of peak force to mean force.

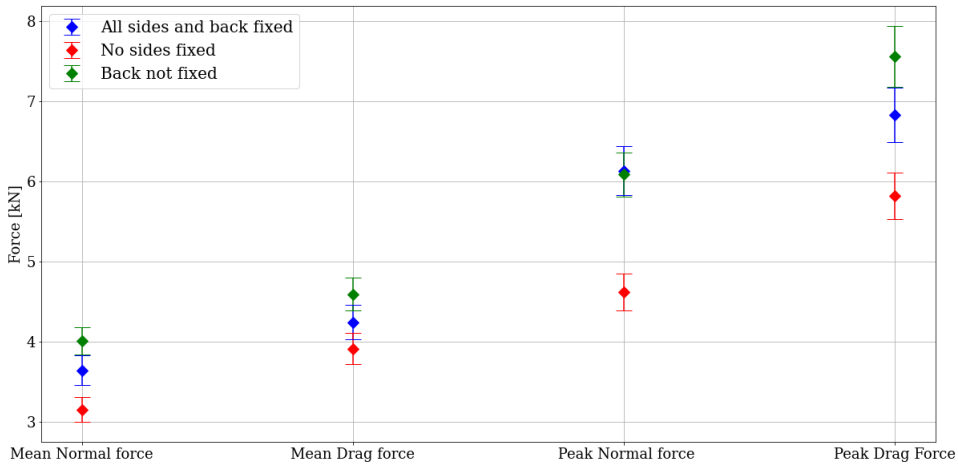

Figure 2.14: Results of different boundary conditions.

Table 2.7: Results of peak force to mean force ratio of different boundary conditions.

Boundary condition	Normal force ratio	Drag force ratio
All sides and back fixed	1.68	1.61
No sides fixed	1.47	1.49
Back not fixed	1.62	1.85

The boundary conditions have a clear influence on both the force results and the peak force to mean force ratio. The most realistic boundary condition is where all the sides and back are fixed. Also the face of the rock is fixed along the z-axis.

The `ERODING_SURFACE_TO_SURFACE`, that is used in the model for the contact between the rock and the pick and the rock and the rock, has three parameters that can be changed: the viscous damping coefficient, the contact penalty scale factor and the target penalty scale factor. All three parameters were changed to the same three different values 10, 5 and 1 to determine the effect.

Figure 2.15 shows the results for the different penalty values, with a 5% error band. Table 2.8 shows the results for the ratio of peak force to mean force.

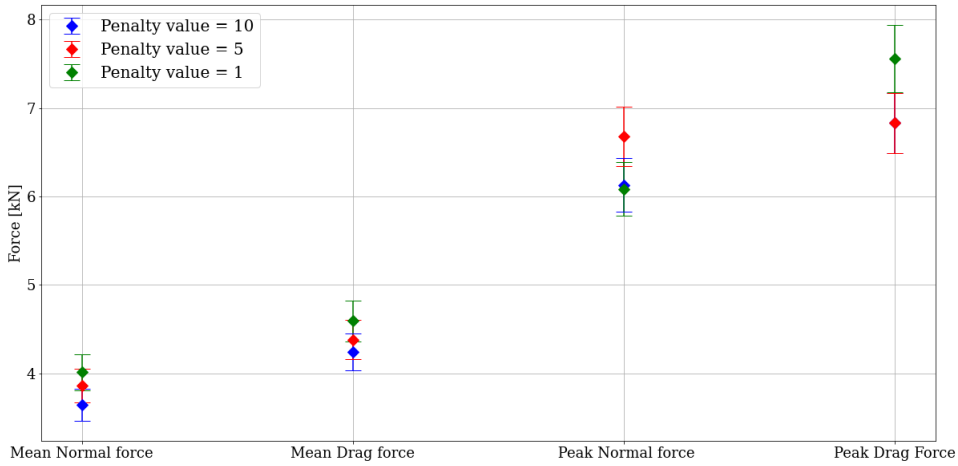

Figure 2.15: Results of different penalty values.

Table 2.8: Results of peak force to mean force ratio of different penalty values.

Penalty value	Normal force ratio	Drag force ratio
10	1.68	1.61
5	1.73	1.56
1	1.52	1.65

The change in penalty value does have a consistent influence on the force results. The mean forces remain constant, but the difference in peak normal force and peak drag force are different for the different penalty values. With a penalty of 1 the difference is the largest and for a value of 5 the difference is the lowest. The ratio of peak force to mean force also changes for the different penalty values. For these tests the element size of the rock was 0.9 mm and the cutting depth 3 mm.

For `ERODING_SURFACE_TO_SURFACE` it must be specified if the contact is frictional or non-frictional. If the contact is frictional the values for the friction coefficient and dynamic coefficient need to be determined. Three different combinations of values were investigated and also non-frictional contact. The initial values were obtained from (Jaime, 2011). Table 2.9 shows the different value combinations.

Table 2.9: Different value combinations for friction coefficient and dynamic coefficient.

Run	Friction coefficient	Dynamic coefficient
1	0.6	0.2
2	1.2	0.4
3	1.6	0.6

Figure 2.16 shows the results of the different combinations of friction coefficient and dynamic coefficient values and non-frictional contact. Table 2.10 shows the peak force to mean force ratio.

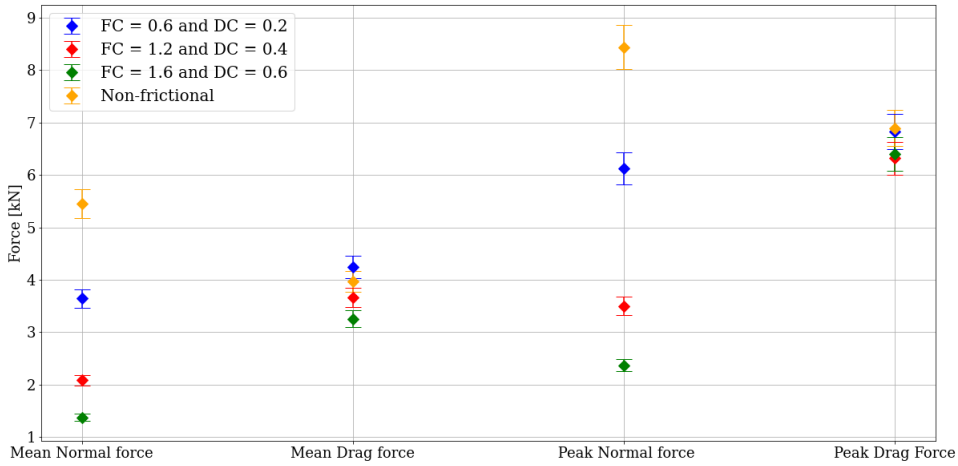

Figure 2.16: Results of different combinations of friction coefficient and dynamic coefficient values and non-frictional contact.

Table 2.10: Results of peak force to mean force ratio of different combinations of friction coefficient and dynamic coefficient values and non-frictional contact.

FC	DC	Normal force ratio	Drag force ratio
0.6	0.2	1.68	1.61
1.2	0.4	1.68	1.72
1.6	0.6	1.72	1.96
Non-fictional		1.55	1.74

From figure 2.16 we see that as the values for the friction coefficient and dynamic coefficient increase the difference between both the mean and peak normal force to the mean and peak drag force increases. The values also have an influence on the peak to mean force ratios. The non-frictional contact is the only contact where, for both peak and mean forces, the normal force has a higher magnitude than the drag force. Thus for the final simulation parameters the friction coefficient and dynamic coefficient will be changed so that the simulated force represents the experimental results as close as possible.

The last CSCM parameter that was investigated was *recov*, stiffness recovery. This will influence the recovery of stiffness and strength when the pressure becomes compressive. For all the tests the *recov* was set at 10.5 meaning 50% of recovery of stiffness and strength when the pressure becomes compressive. It was investigated what would be the influence on the force values as well as the force signal if the *recov* is set to zero or 1.

Figures 2.17 and 2.18 show the signal of the normal force and drag force for the different *recov* values. Only the force signal was looked at because the mean and peak force values were not influenced by the change in *recov* value.

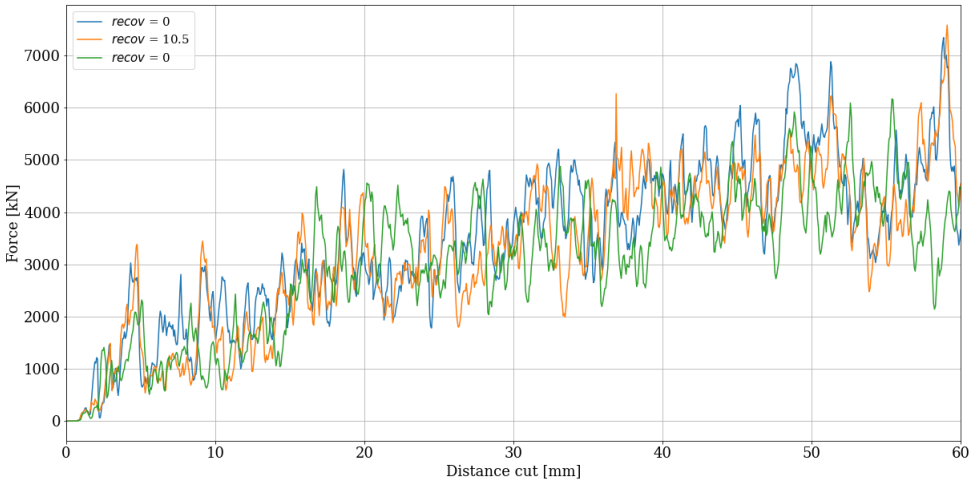

Figure 2.17: Normal force signal for different *recov* values.

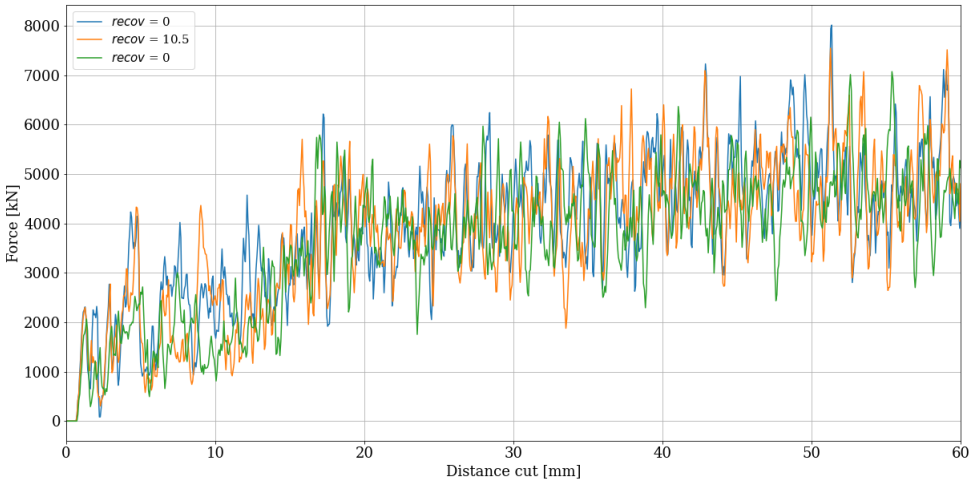

Figure 2.18: Drag force signal for different *recov* values.

The figures show that the different *recov* values do not have an impact on the force signals.

Different mesh types were investigated to determine the influence on the force signals and the peak to mean force ratio. Three different mesh types found in Ansys were investigated. The mesh types were tetrahedrons, hexahedron and cartesian. Figure 2.19 shows the normal force signals for the different mesh types and figure 2.20 shows the drag force signals.

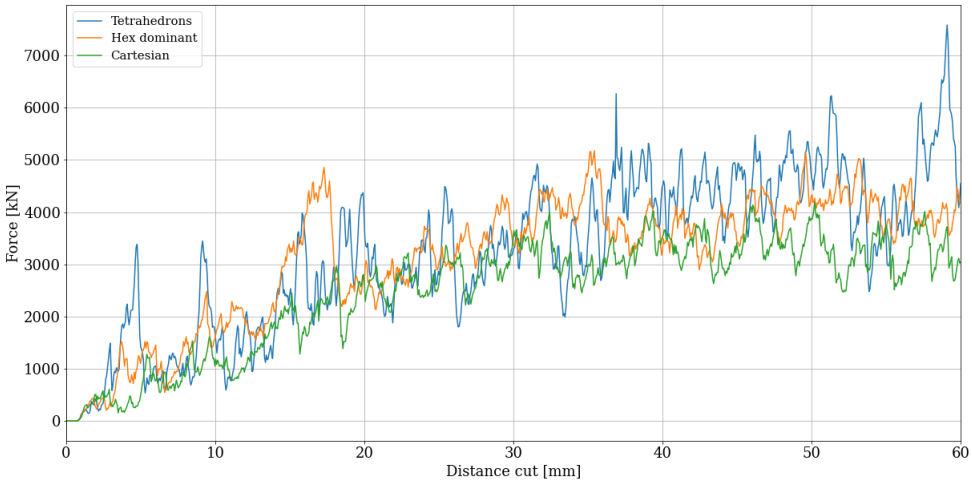

Figure 2.19: Normal force signal for different mesh types.

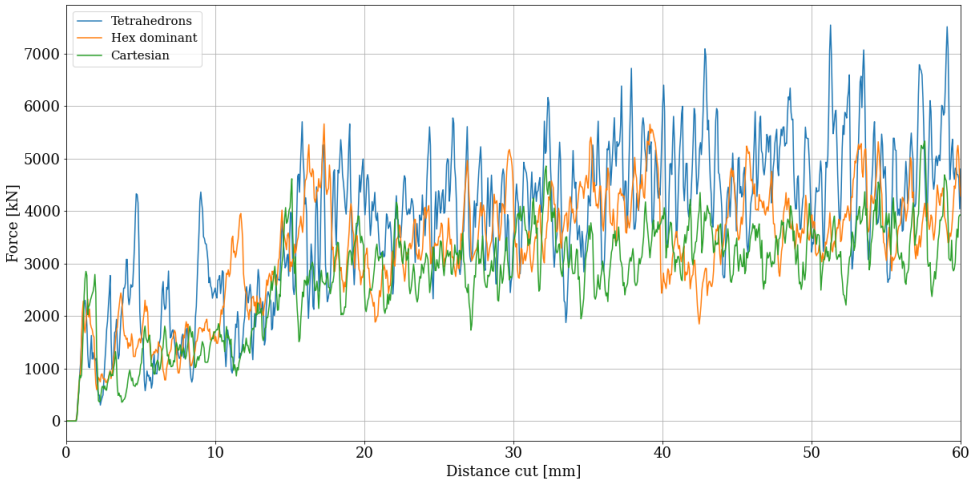

Figure 2.20: Drag force signal for different mesh types.

From the force signals it is clear the mesh type does not have a big influence. But the force signal of the tetrahedron mesh type is more impulsive than the other mesh types.

In the study of the model set-up it is clear that there are various choices that need to be made and various parameters that need to be set and determined. Some of the choices and parameters have an influence on the model results and some do not.

The choices and model parameters that are chosen for the final numerical simulations, to simulate rock cutting of UG2 reef samples, are shown and motivated in section 4.4.

Chapter 3

Linear cutting machine

Chapter 3 presents the requirements of the linear cutting machine so that the laboratory cutting tests can be performed. The chapter also shows the design and manufacturing of the linear cutting machine. The design, manufacturing and calibration of the load cell that was used by the linear cutting machine is also shown in the chapter.

The chapter covers the testing of the linear cutting machine using sandstone samples to ensure that the linear cutting machine works as expected.

3.1 Linear cutting machine design

The study utilizes a linear cutting machine (LCM) that incorporates various design requirements and considerations. The LCM must possess sufficient strength and stability to endure the cutting forces experienced in all three orthogonal directions. Additionally, it should facilitate a linear motion to enable the movement of either the conical pick or the rock specimen, thus simulating the cutting process. Furthermore, the machine should be equipped with the capability to measure the three orthogonal cutting forces, these requirements were determined from sections 1.4.6 and 1.4.9. This enables a comparison of different cutting parameters and numerical simulations.

To ensure flexibility of the cutting parameters, the LCM must be constructed in a manner that allows for accurate adjustments of the depth of cut, attack angle, skew angle, and cut spacing, as dictated by the specific requirements. After each cut, it is essential to collect the rock chips for weighing purposes to determine the specific energy required per cut. Consequently, the LCM should be designed to facilitate the collection of these rock chips rather than allowing them to simply fall to the ground.

Figure 3.1 shows the degrees of freedom required of the LCM.

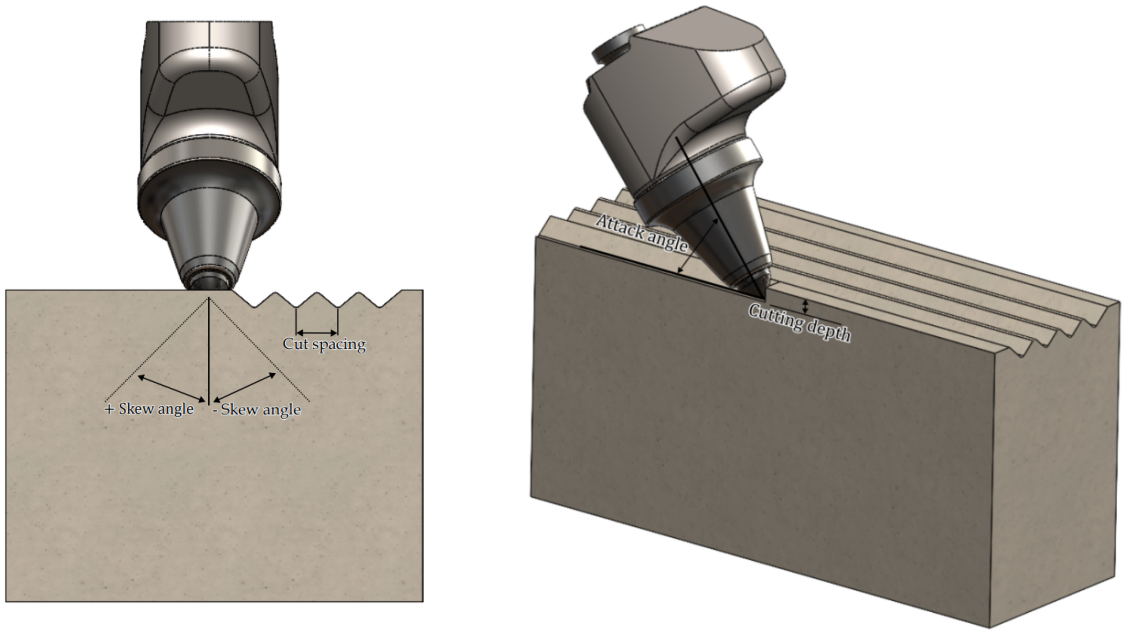

Figure 3.1: Degrees of freedom required of the LCM.

For this study a radial arm drilling machine was modified so that it meets all the requirements of the LCM. Figure 3.2 shows both the CAD of the LCM and the actual LCM.

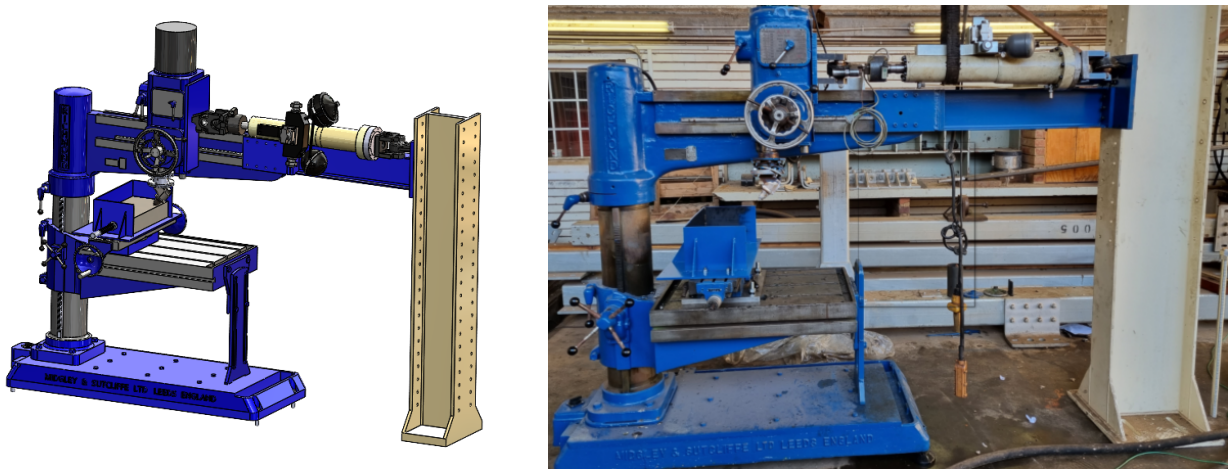

(a) CAD of LCM. **(b)** Actual LCM.

Figure 3.2: LCM used in this study.

As stated above the LCM must meet various design requirements. The LCM has different components that fulfil different requirements. Figure 3.3 shows the different components of the LCM.

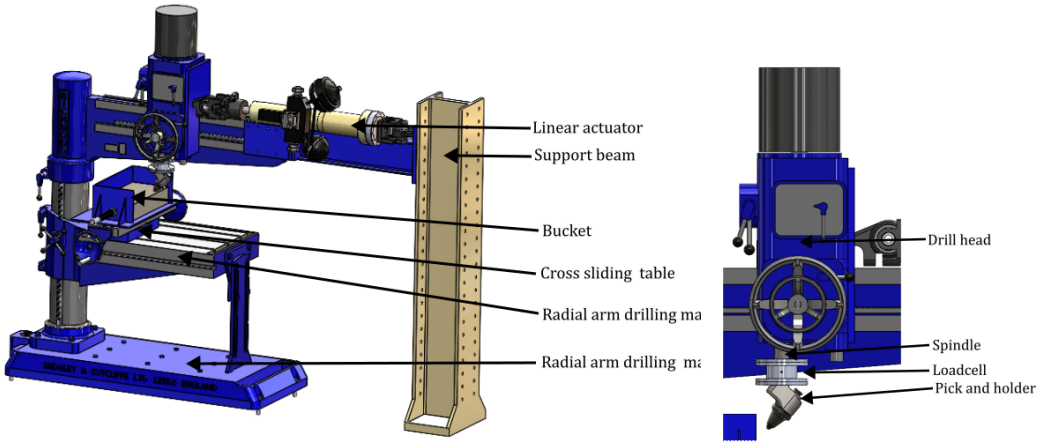

(a) Full view of LCM. **(b)** Drill head assembly.

Figure 3.3: Different components of the LCM.

The different components translate in different directions to meet the requirements. Figure 3.4 shows how the different components of the LCM can move.

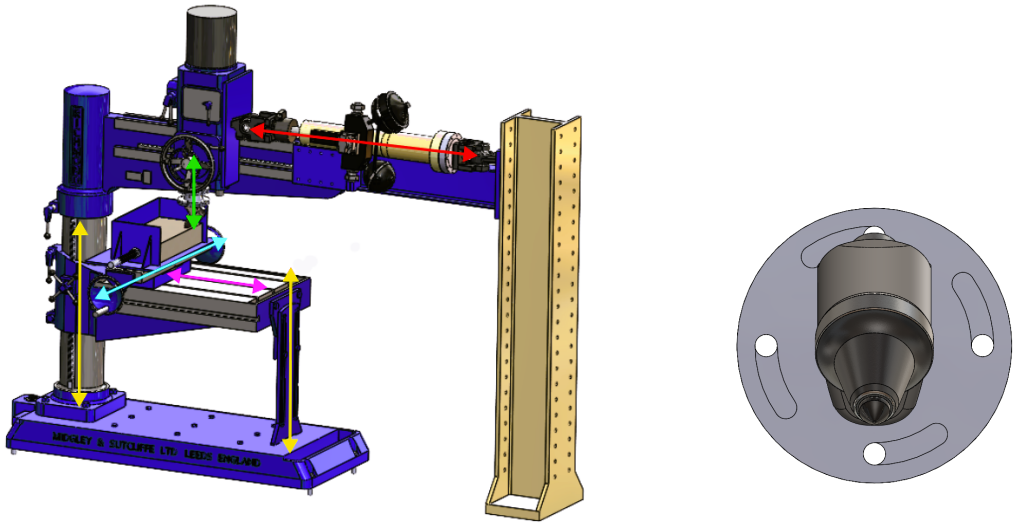

(a) Full view of LCM. **(b)** Load cell assembly.

Figure 3.4: Movement of different components of the LCM.

The linear actuator moves horizontally as shown by the red arrow. This horizontal movement simulates the cutting motion by pressing the pick through the rock. The linear actuator has a maximum horizontal movement of 240 mm. The speed at which it cuts can be adjusted.

The radial arm drilling machine table allows for both horizontal and vertical movement. The vertical movement is shown by the yellow arrows. This allows for large vertical movement. The table allows the cross sliding table to move horizontally as shown by the pink arrow. Both the horizontal and

vertical movement is used to move the rock specimen into the correct position.

The cross sliding table allows for accurate changes in cut spacing shown by the light blue arrow. The spindle can move vertically, which allows for accurate changes to the cutting depth shown by the green arrow. Figure 3.4b shows the slots that are cut in the lower flange of the load cell assembly. These slots allow for change in the skew angle. The skew angle can be adjusted to a maximum of 30°. The attack angle can be changed by changing the bottom flange and pick holder.

The bucket can hold a rock specimen with maximum dimensions 500 mm wide, 250 mm long and 200 mm high. The bucket has a clamp that clamps the rock specimen into place. The support of the LCM is bolted to the ground. Because the LCM works as a press, all the forces act on the machine and not on the support. The support only gives stability.

Figure 3.5 shows the conical pick used in the laboratory scale cutting tests. The pick is a TS31CX conical pick supplied by Kennametal South Africa (Pty) Ltd.

Figure 3.5: Conical pick used in this study.

Figure 3.6 shows the dimensions of the conical pick used in the laboratory scale cutting tests. The dimensions were used to make CAD drawings of the conical pick, which was later used for the numerical simulations. The dimensions were measured by hand due to the design being intellectual property of Kennametal South Africa (Pty) Ltd.

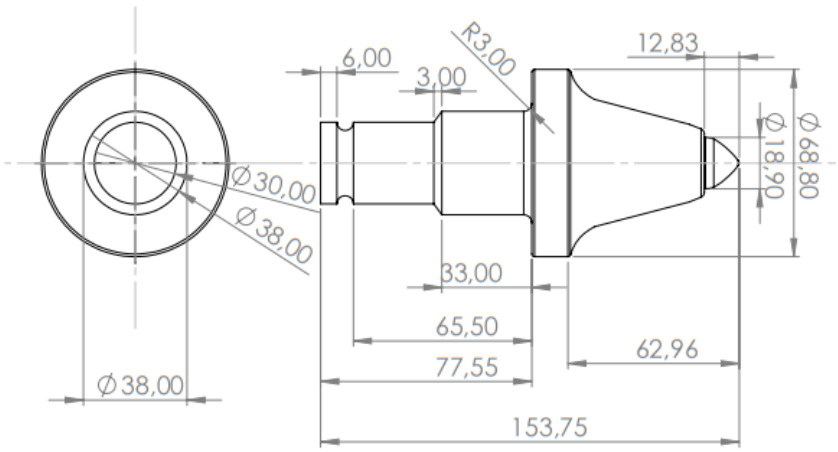

Figure 3.6: Dimensions of conical pick used in this study, in mm.

The LCM used in this study fulfils all the requirements needed to perform the experimental tests.

3.2 Load cell

The study requires that the load cell measures all three orthogonal forces, drag force, normal force and side force as shown in figure 3.7. These forces will be used to determine the cut-ability of the rock as well as other measurements such as specific energy.

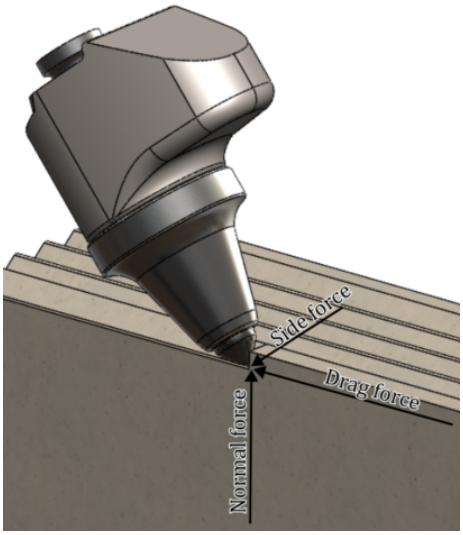

Figure 3.7: Three orthogonal cutting forces.

For the study a load cell was designed and manufactured that uses four half bridge strain gauges that are equally spaced around the circumference of a circular steel tube. Figure 3.8a shows the load cell assembly and figure 3.8b shows the load cell only. The load cell is calibrated directly to the applied force. The rest of the section describes the design and calibration of the load cell used in the study.

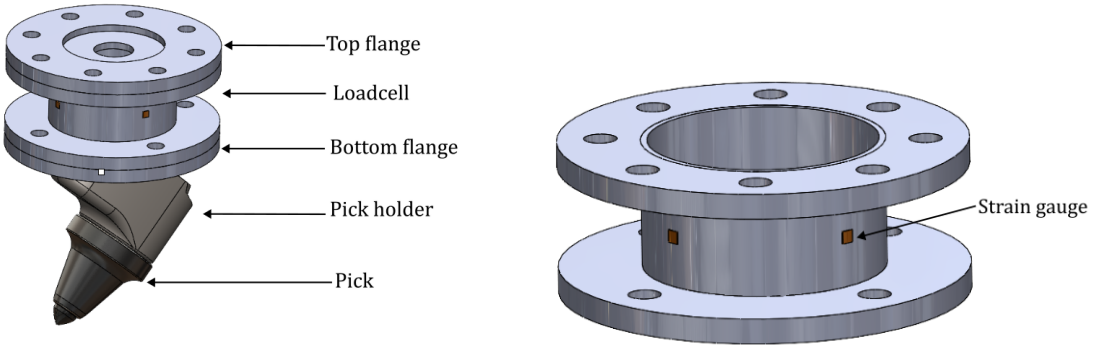

(a) Load cell assembly. **(b)** Load cell.

Figure 3.8: Load cell assembly and load cell.

3.2.1 Load cell design

The design of the load cell works on the principle of a cantilever beam. The load cell assembly can be seen as a cantilever beam with three different forces acting at the tip of the cantilever beam. The beam deforms due to the forces acting on the beam. These deformations can be measured and related to applied forces.

The load cell for this study uses a circular tube for the beam. As the tube deforms four half bridge strain gauges measure the deformation. The load cell has only two parameters that can be changed. This is the inner and outer diameters of the tube. The length of the tube was selected that there is adequate space to place the strain gauges.

Figure 3.9 shows the free body diagram of the load cell. The bending arms, L and S are fixed due to the size of the pick and the pick holder, the size of steel plates used to make the flanges and the length of the circular tube that is used for the load cell.

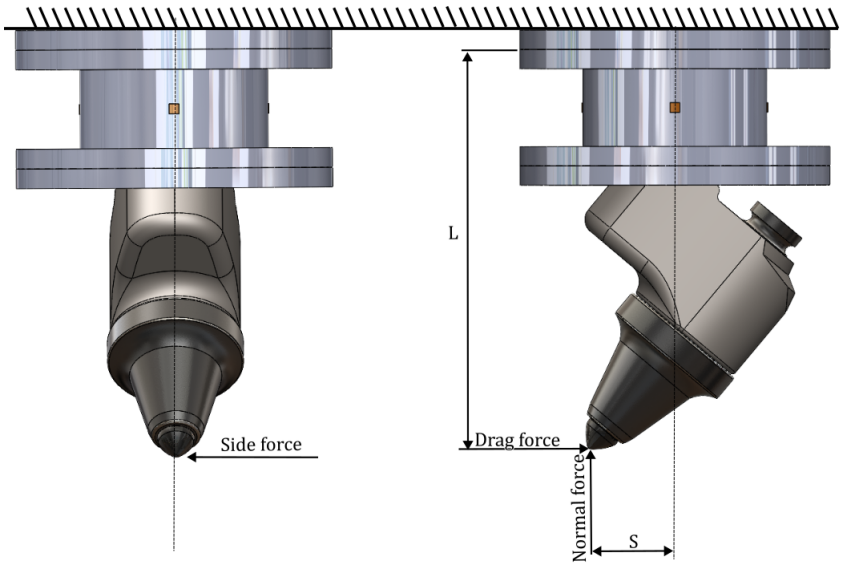

Figure 3.9: Free body diagram of the load cell.

The diameter of the round tube is also limited. The limits are based on the size constraints of the available material, the available space on the LCM and the machining limitations available at the university. The material used for the round tube is EN24 with a Young's modulus of 207 GPa and Poisson's ratio of 0.33.

The available material had a diameter of 105 mm. The available space on the LCM allows for the load cell flanges to have a maximum outer diameter of 170 mm. The machining limitations available at the University allows the minimum wall thickness to be 2.5 mm.

To determine the dimensions for the load cel, cantilever beam calculations were performed. The applied forces that were used for the calculations were taken from (Su and Akcin, 2011). (Su and Akcin, 2011) give us a drag force of 20 kN, a normal force of 20 kN and a side force of 5 kN. These forces were used because it ensures that the load cell can handle a wide range of forces.

If the forces for the calculations are chosen too low, the load cell will plastically deform and thus be unusable. The magnitude of the forces was determined from experimental results of cutting different types of sandstone and limestone at different cutting depths (Su and Akcin, 2011). The uniaxial compressive strength of the rock cut in the experiments range from 85 MPa to 175 MPa. Thus, the uniaxial compressive strength of the UG2 reef rock falls in the range. The cutting depths were 3 mm, 6 mm and 9 mm.

During the calculations the strain due to the forces were determined individually. It is clear that the drag force and side force will cause bending in the beam with a bending arm of length L. The normal force will cause compression and bending in the beam but with a short bending arm of S. Because the load cell will be calibrated directly to applied force the design of the load cell should just ensure that it meets all limitations and have a good sensitivity.

It was decided that the outer diameter will be 95 mm and the inner diameter will be 90 mm. These dimensions meet all the limitations for the manufacturing of the load cell. The following calculations show that the load cell with these dimensions does not plastically deform when the forces are applied and that a good sensitivity is achieved.

For the calculations the following forces, design parameters and material properties were assumed:

- $D_o = 95\,mm$
- $D_i = 90\,mm$
- $L = 195\,mm$
- $S = 45\,mm$
- $E = 207\,GPa$
- $\nu = 0.33$
- $F_{drag} = 20\,kN$

- $F_{norm} = 20\,kN$
- $F_{side} = 5\,kN$

where D_o is the outer diameter, D_i is the inner diameter, L and S are the dimensions shown in figure 3.9, E is the Young's modulus, ν is the Poisson's ratio, F_{drag} is the drag force, F_{norm} is the normal force and F_{side} is the side force as applied in figure 3.9.

Equation 3.1 was used to determine the second moment of inertia of the circular tube, equation 3.2 the area of the cross section of the tube, 3.3 the moment that will be experienced, equation 3.4 and 3.5 the stress and equation 3.6 the strain due to each force.

$$I = \frac{\pi}{64}\left(D_o^4 - D_i^4\right) \tag{3.1}$$

where D_o is the outer diameter, D_i is the inner diameter.

$$A = \frac{\pi}{4}\left(D_o^2 - D_i^2\right) \tag{3.2}$$

$$M = Fd \tag{3.3}$$

where F is the applied force and d is the perpendicular distance of the line of action of the force from the point where the moment is calculated.

$$\sigma_{bending} = \frac{My}{I} \tag{3.4}$$

where M is the moment, y is the outer radius of the tube because that is where the stress will be the largest and I the second moment of inertia of the circular tube.

$$\sigma_{compression} = \frac{F}{A} \tag{3.5}$$

where F is the applied force and A is the area of the cross section of the tube.

$$\varepsilon = \frac{\sigma}{E} \tag{3.6}$$

where σ is the stress and E is the young's modulus.

Using the equations and substituting in the unknowns, table 3.1 show the resultant micro strain that will be achieved for the applied forces. The results show that the load cell will be more sensitive in bending as expected. The load cell will also be capable of withstanding a range of forces before the load cell plastically deforms.

Table 3.1: Load cell design calculation results

	Normal force compression	Normal force bending	Drag force bending	Side force bending
M [Nm]		900	3900	975
A [m^2]	7.26e-4			
I [m^4]		7.78e-7	7.78e-7	7.78e-7
Stress [MPa]	27.53	54.98	238.24	59.56
Micro strain	132.99	265.60	1150.92	287.73

3.2.2 Load cell calibration

The load cell was calibrated by measuring the strain gauge output for an applied force. The force was applied so that a combination of orthogonal forces were applied. This was done because when cutting the rock, a combination of orthogonal forces will be applied to the load cell.

The application of a combination of orthogonal forces was done by pressing the point of the conical pick with a hydraulic jack and measuring the applied force. Two different combinations of forces were applied. The first was a combination of drag force and normal force and the second was normal force and side force.

For the calibration of the combination of the drag force and normal force, three different calibration datasets at three different angles were obtained, giving nine datasets. Figure 3.10 shows the set-up for the calibration. A calibrated load cell as shown in figure 3.10 was used to determine the applied force, then the applied load was split into a drag force and a normal force, based on the angle of the hydraulic jack.

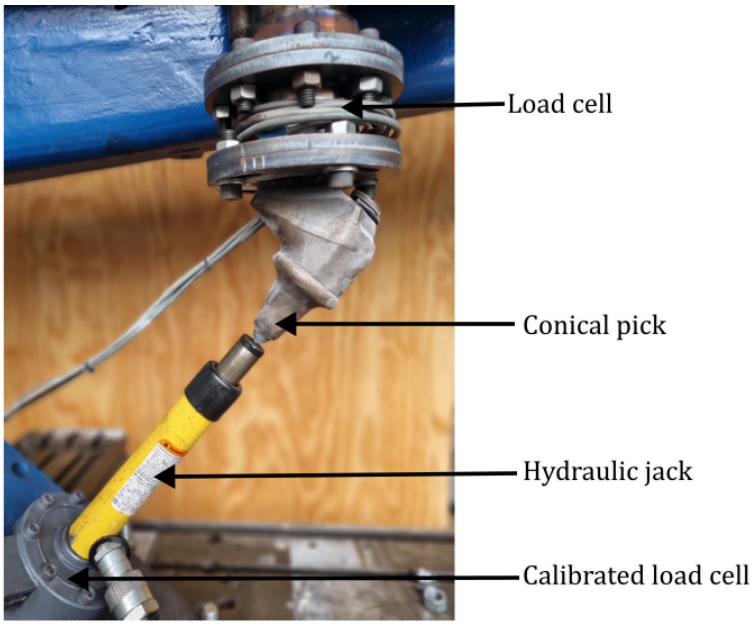

Figure 3.10: Combination of drag force and normal force.

For the calibration of the combination of the normal force and side force, three different datasets at two different angles were obtained giving six datasets per side. The calibration of the combination of the normal force and side force was done in both directions of the side force giving twelve datasets. Figure 3.11 shows the set-up for one of the directions in which the combination of the normal force and side force was calibrated. The applied force was split into the two applied forces the same as with the calibration of the combination of the drag force and normal force.

Figure 3.11: Combination of drag force and normal force.

The twenty one calibration datasets give five thousand five hundred and nineteen calibration points. These calibration points are used to calibrate linear equations to predict the three orthogonal forces. Linear equations are used due to the linear relationship between strain and applied force in the elastic deformation range.

The load cell gives four measurements. It is the four values measured by the half bridge strain gauges. These values are used in the linear equations as shown in equations 3.7 to 3.9.

$$F_{Normal} = A_1 \left(A_2 SG_1 + A_3 SG_3 + 2\left(A_4 SG_2 + A_5 SG_4\right)\right) \tag{3.7}$$

$$F_{Drag} = A_6 \left(A_7 SG_1 - A_8 SG_3 + 2\left(A_9 SG_2 + A_{10} SG_4\right)\right) \tag{3.8}$$

$$F_{Side} = A_{11} \left(A_{12} SG_4 - A_{13} SG_2\right) \tag{3.9}$$

where F_{Normal} is the predicted normal force, F_{Drag} is the predicted drag force, F_{Side} is the predicted side force and SG_1 to SG_4 are the four strain gauge values where SG_1 is the value from the front strain gauge and the rest of the strain gauges are numbered anti-clock wise when looking at the top

of the load cell, as shown in figure 3.12.

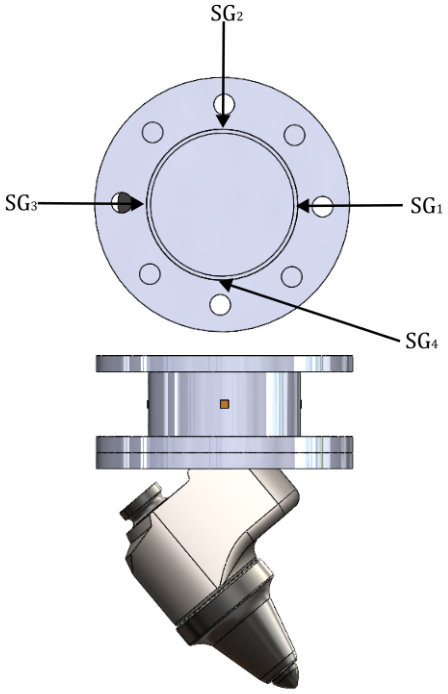

Figure 3.12: Strain gauge positions

A_1 to A_{13} are coefficients that were determined by minimizing the mean squared error (MSE) for the calibration data, table 3.2 shows the values for the coefficients. For the minimising `scipy.optimize.minimize` was used with Broyden–Fletcher–Goldfarb–Shanno (BFGS) as the method of minimization. The MSE is defined by equation 3.10.

$$MSE = \frac{\sum \left(x - x_{pred}\right)^2}{n} \tag{3.10}$$

where x is the actual value, x_{pred} is the predicted value and n is the number of samples.

Table 3.2: A_1 to A_{13} coefficients

Coefficients												
A_1	A_2	A_3	A_4	A_5	A_6	A_7	A_8	A_9	A_{10}	A_{11}	A_{12}	A_{13}
-0.0516	1.2500	1.1246	0.4677	0.5471	-0.0194	1.4684	0.1801	0.0830	0.1039	-0.0236	0.6148	0.9339

Table 3.3 shows the absolute mean error of the linear equations for the normal force, drag force and side force. The table shows both the mean and standard deviation.

Figure 3.13 shows the predicted value versus the actual value for the linear equations.

Table 3.3: Absolute mean error of the linear equations

Absolute mean error			
	Normal force	Drag force	Side force
Mean	0.035353	0.017914	0.025796
Standard deviation	0.028174	0.023471	0.018905

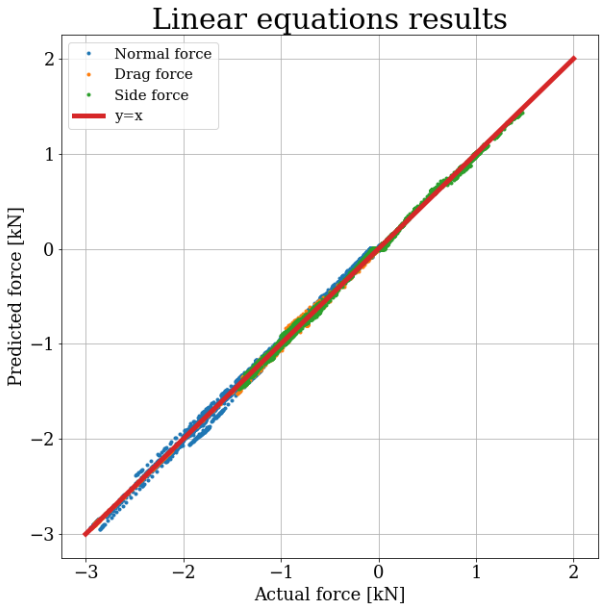

Figure 3.13: Linear equation results.

From table 3.3 and figure 3.13 it is clear that the linear equations predict the forces with acceptable accuracy.

3.3 Linear cutting machine testing

To ensure that the LCM functions as expected, the LCM was first tested by cutting sandstone. The rock properties of the sandstone are shown in table 3.4. This also tested the cutting sequence that will be used when cutting the UG2 rock sample. Various cutting tests with different parameters were conducted on the sandstone.

Table 3.4: Sandstone rock properties.

Material	Young's Modulus E [GPa]	Poisson's ratio ν	Density ρ [g/cm^3]	Compressive strength [MPa]
Sandstone	14.8	0.45	2.33	55.5

In the tests the cutting depth, the cut spacing and the skew angle were changed. The tests were performed at cutting depths of 2 mm and 4 mm. The cut spacing was changed so that the cut spacing to cutting depth ratio was 1,2,3,4,5 and 6. The skew angle was changed from $-10°$, $0°$ and $10°$. The attack angle was kept constant at $50°$.

The cutting speed was the same for all the tests at 50 mm/s and sampling rate of 300 Hz was used for all the tests, for the strain gauge measurements.

A cutting sequence consisted out of firstly pre-cutting the surface to simulate a rock face and then nineteen cuts. The first cut was an initial cut then three of each ratio was cut starting at a ratio one to six. After each cut the cut material was collected and weighed. The weighed mass and the density of the material were used to determine the specific energy.

Figure 3.14a shows the pre-cut area and the cut area, for 2 mm cutting depth. Figure 3.14b shows the cutting sequence. In the cutting sequence the black line is the initial cut, the pink is the first three cuts at a cut spacing of 2 mm, the turquoise lines are at a cut spacing of 4 mm, the yellow lines are at a cut spacing of 6 mm, the green lines are at a cut spacing of 8 mm, the blue lines are at a cut spacing of 10 mm and the red lines are at a cut spacing of 12 mm. The cutting sequence starts from the black line and ends at the top red line.

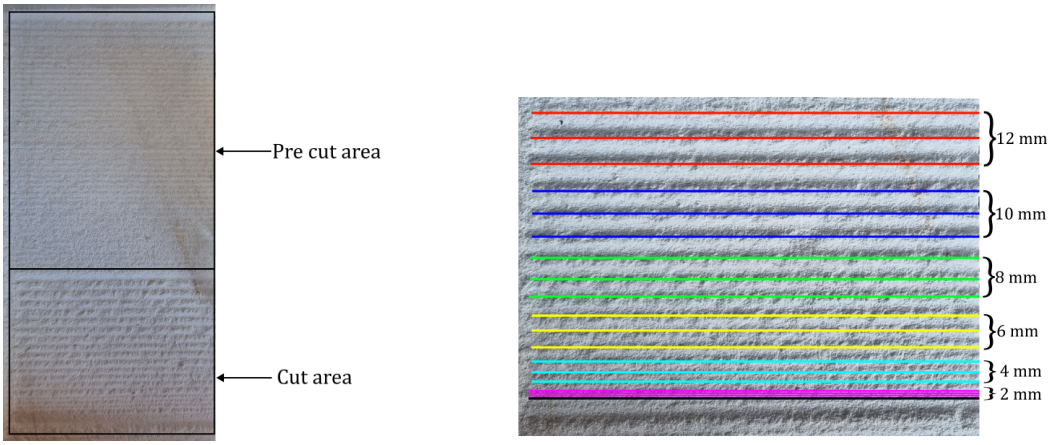

(a) Pre-cut and cut area of sandstone.

(b) Cutting sequence.

Figure 3.14: Cut sandstone.

3.3.1 Results

The results of the tests show the mean cutting forces, peak cutting forces and the specific energy versus the cut spacing to cutting depth ratio. The cut spacing to cutting depth ratio was used to display the data because it is a dimensionless quantity. Thus different cutting depths can be compared to one another. Also from sections 1.4.6 and 1.4.9 it is the norm for displaying the results. The graphs show the average value as well as the maximum and minimum value, this shows the uncertainty in the data.

When looking at the results of the side forces, especially the peak side force, it must be noted that at large cut spacing to cutting depth ratios the mean is close to zero. Thus the peak value will either be positive or negative so when looking at the peak side force results the magnitude is the important value, not the sign. Figure 3.7 show the forces in the positive direction. Also the sign of the side force is dependent on the direction of the cutting sequence. For positive and negative skew angle the sign differs as expected, because the cutting sequence is run in different directions. But the direction

of the cutting sequence for zero skew angle is the same as for negative skew angle. This is something that has to be acknowledged when looking at the results of the side forces.

Figures 3.15 and 3.16 show the mean normal force for 2 mm cutting depth and 4 mm cutting depth.

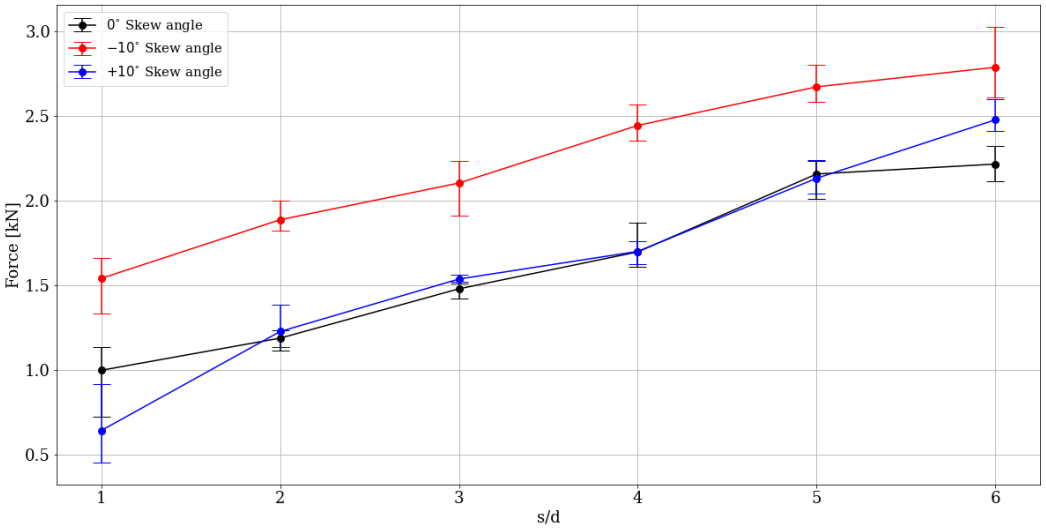

Figure 3.15: Mean normal force for 2 mm cutting depth.

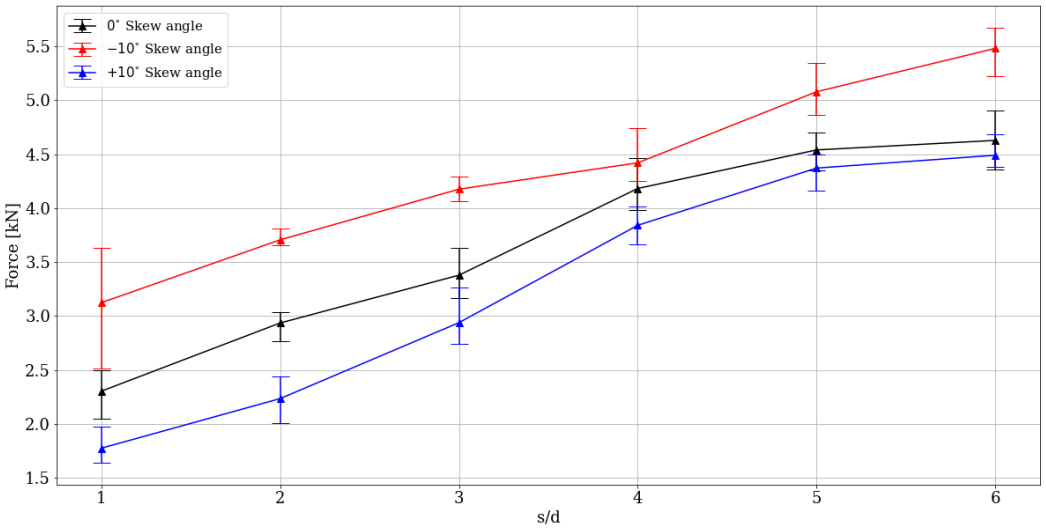

Figure 3.16: Mean normal force for 4 mm cutting depth.

Figures 3.15 and 3.16 show that the same trend is followed for both cutting depths. The mean normal force increases as the cut spacing to cutting depth ratio increases. The increase is almost linear.

For both cutting depths, a skew angle of $-10°$ requires a larger mean normal force. This does not

influence the specific energy as the specific energy relies on the drag force, cut distance and volume of cut material.

Figures 3.17 and 3.18 show the mean drag force for 2 mm cutting depth and 4 mm cutting depth.

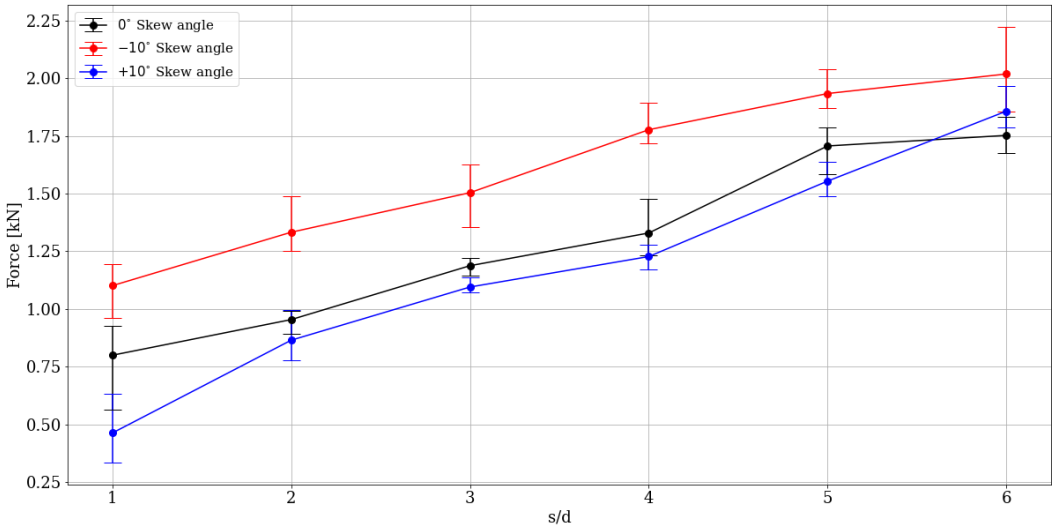

Figure 3.17: Mean drag force for 2 mm cutting depth.

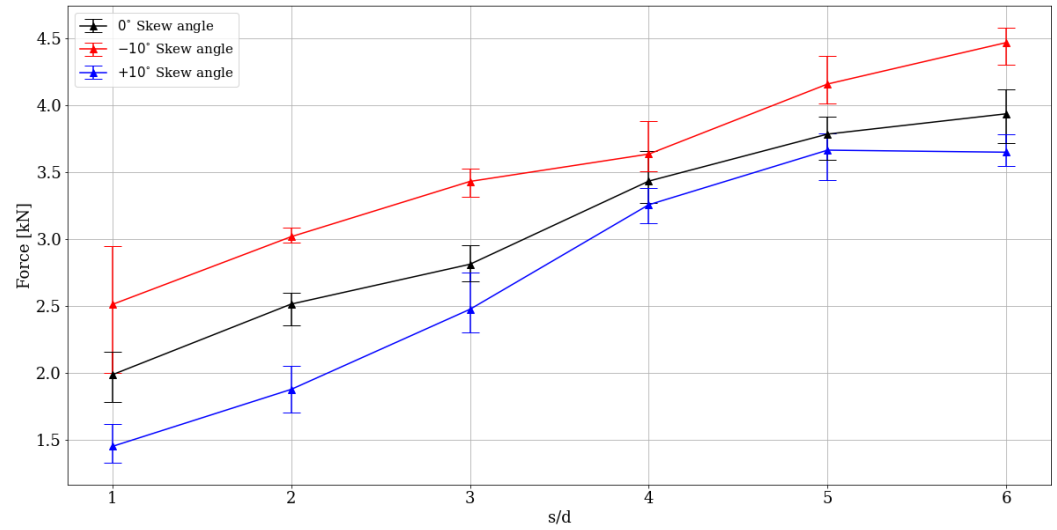

Figure 3.18: Mean drag force for 4 mm cutting depth.

Figures 3.17 and 3.18 show that the same trend is followed for both cutting depths. The mean drag force increases as the cut spacing to cutting depth ratio increases. The increase is almost linear.

For both cutting depths, a skew angle of $-10°$ requires a larger mean drag force. This influences the

specific energy as the specific energy relies on the drag force.

Figures 3.19 and 3.20 show the mean side force for 2 mm cutting depth and 4 mm cutting depth.

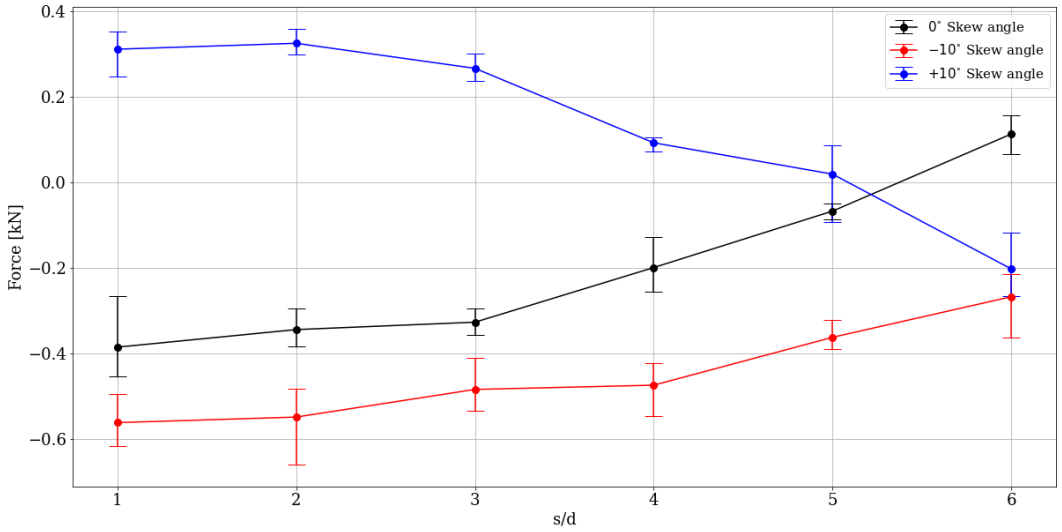

Figure 3.19: Mean side force for 2 mm cutting depth.

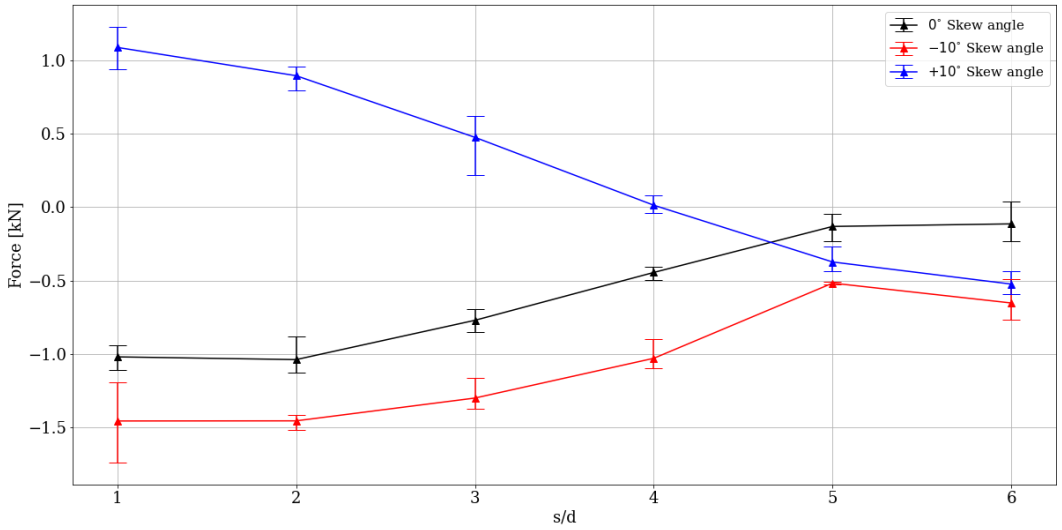

Figure 3.20: Mean side force for 4 mm cutting depth.

Figures 3.19 and 3.20 show that the mean side force has the same trend for both cutting depths. The mean side force, for the -10° skew angle, change direction at $s/d = 5$ and $s/d = 4$ for the 2 mm cutting depth and 4 mm cutting depth. This is interesting because at that s/d ratio the mean of the side force is almost zero which is desirable in the design of the cutting parameters.

The reason for the change in direction is due to the change in frontal area that is in contact with the rock when cutting. Figure 3.21 shows the frontal area when cutting an initial cut. The area on the left, yellow, represents the area of the pick where the rock will apply a force to the right on the pick. The area on the right, blue, represents the area of the pick where the rock will apply a force to the left on the pick. The grey area represents the area of the rock that is being cut. The blue area is larger than the yellow area. Thus, the force to the left is larger for an initial cut.

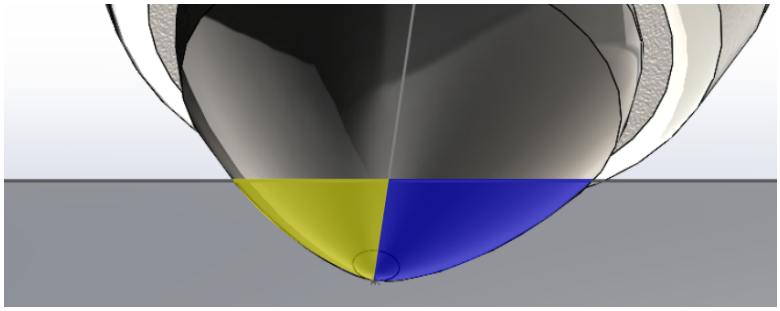

Figure 3.21: Frontal area for an initial cut with a skew angle.

Figure 3.22a shows the frontal area for a small s/d cut with a positive skew angle. The figure shows that there is only an area on the left, yellow, representing the area of the pick where the rock will apply a force to the right on the pick. Thus for the small s/d the force will be to the right. Figure 3.22b shows the frontal area for a large s/d cut with a positive skew angle. The figure shows that there are both a yellow and blue area, that have about the same area. Thus, the forces to the left and the right will cancel one another and the force will be close to zero.

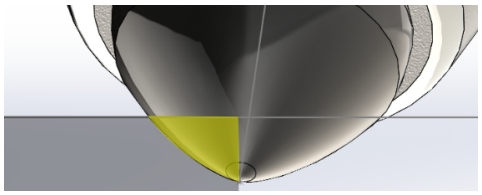

(a) Small s/d cut.

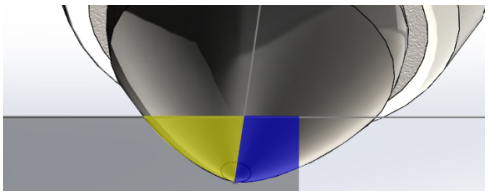

(b) Large s/d cut.

Figure 3.22: Frontal areas for positive skew angle cuts.

Figure 3.23a shows the frontal area for a small s/d cut with a negative skew angle. The figure shows that there is only an area on the right, blue, representing the area of the pick where the rock will apply a force to the left on the pick. Thus for the small s/d, the force will be to the left. Figure 3.23a shows the frontal area for a large s/d cut with a negative skew angle. The figure shows that there are both a yellow and blue area, but the blue area is larger. Thus the forces to the left are larger than the forces to the right so the force applied on the pick will be to the left.

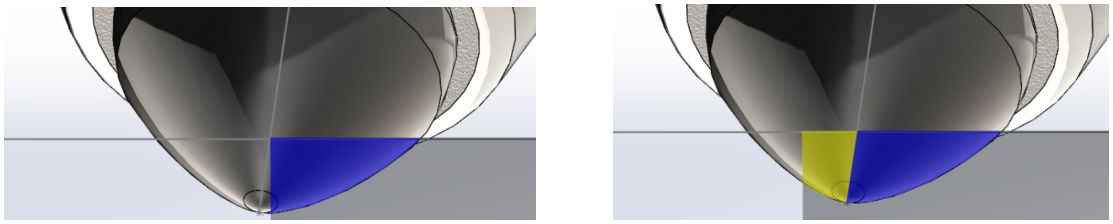

(a) Small s/d cut.

(b) Large s/d cut.

Figure 3.23: Frontal areas for negative skew angle cuts.

This theory about the frontal area of the pick is shown by the results of the mean side forces at different s/d values.

Figures 3.24 and 3.25 show the peak normal force for 2 mm cutting depth and 4 mm cutting depth.

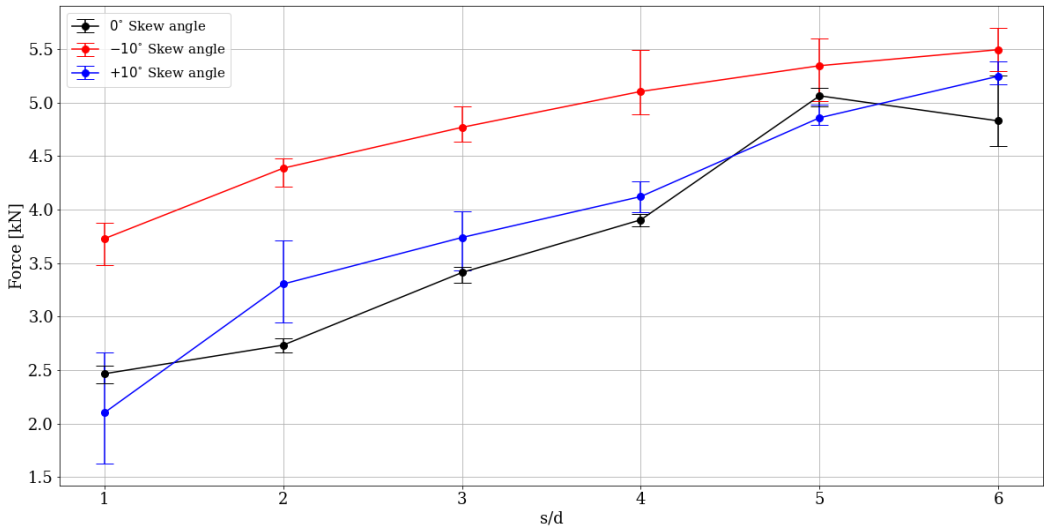

Figure 3.24: Peak normal force for 2 mm cutting depth.

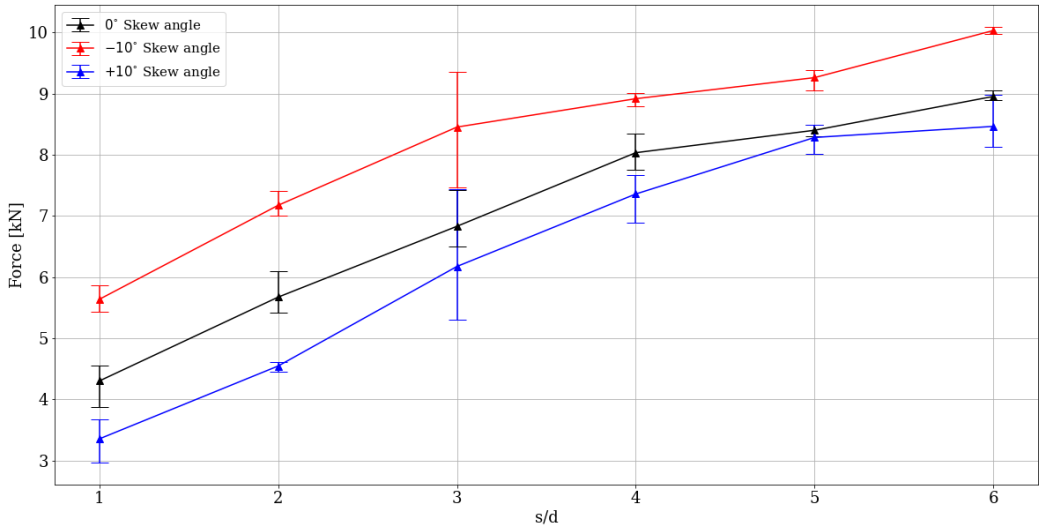

Figure 3.25: Peak normal force for 4 mm cutting depth.

Figures 3.26 and 3.27 show the peak drag force for 2 mm cutting depth and 4 mm cutting depth.

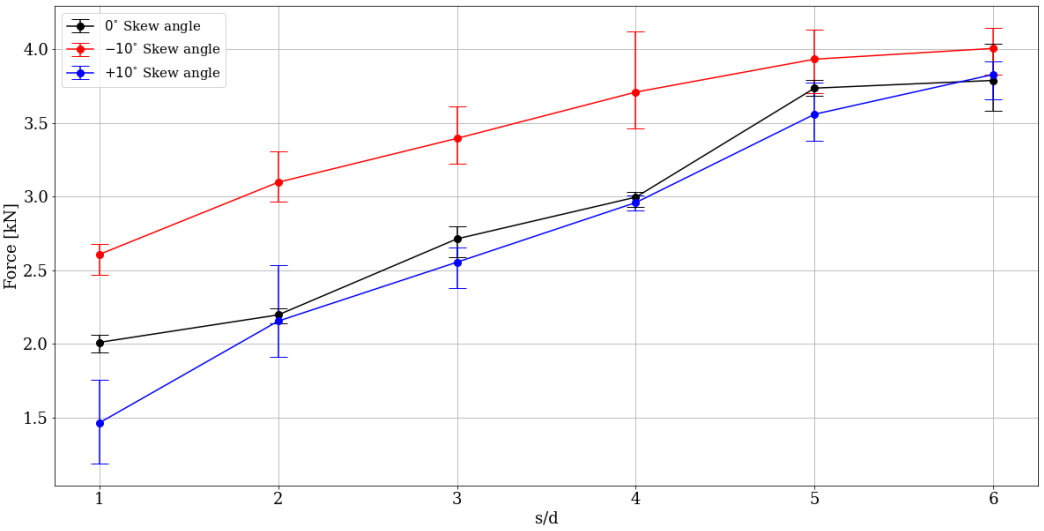

Figure 3.26: Peak drag force for 2 mm cutting depth.

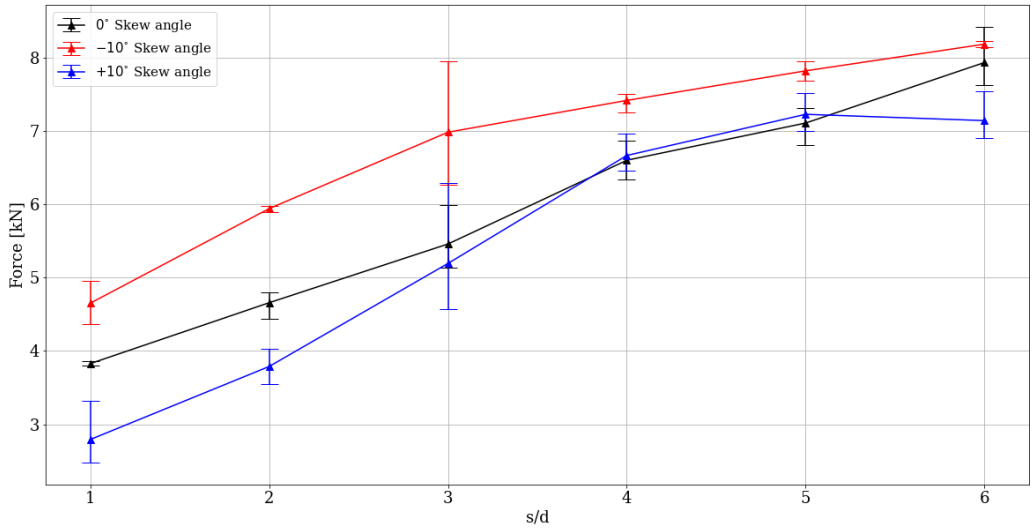

Figure 3.27: Peak drag force for 4 mm cutting depth.

Figures 3.28 and 3.29 show the peak side force for 2 mm cutting depth and 4 mm cutting depth.

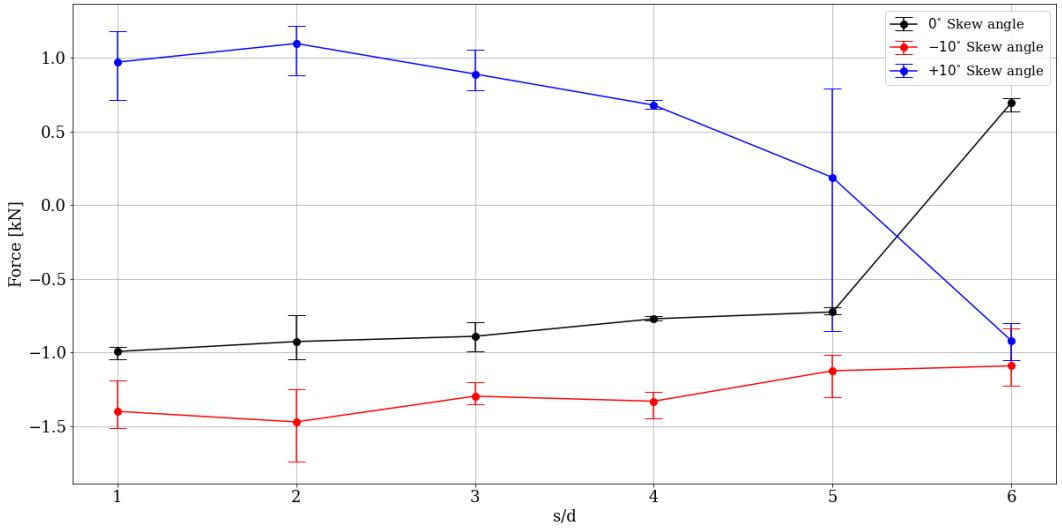

Figure 3.28: Peak side force for 2 mm cutting depth.

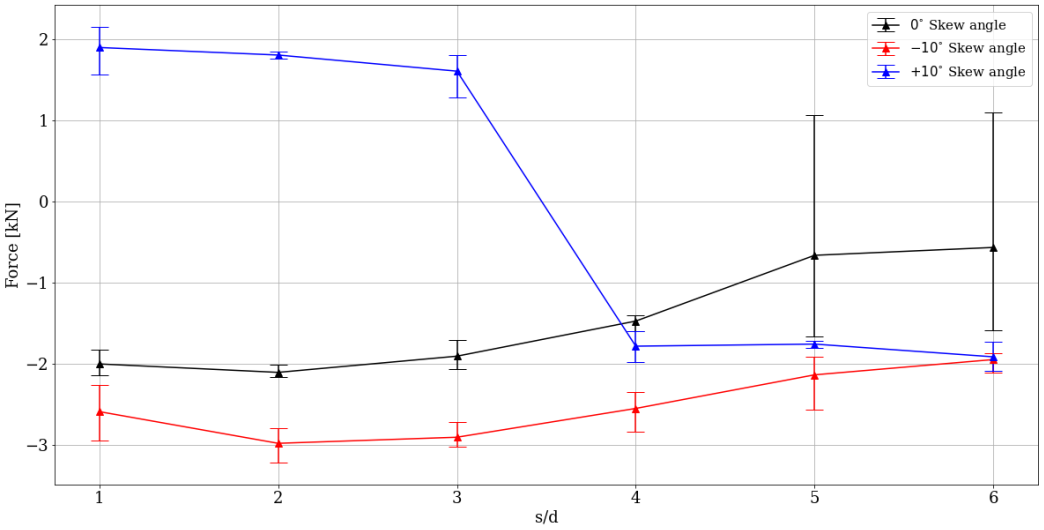

Figure 3.29: Peak side force for 4 mm cutting depth.

The peak forces shown in figures 3.24 to 3.29 show the same trends as their mean force graphs in figures 3.15 to 3.20.

When looking at the cutting force signals, some conclusions can be made. The cutting force signals that are shown in figures 3.30 to 3.33 are all at a s/d of 3, attack angle of 50° and only 100 mm of the cutting is shown. Figures 3.30 to 3.32 are at a cutting depth of 2 mm. Figures 3.33 to 3.35 are at a cutting depth of 4 mm.

The figures show the results for 0° skew angle, −10° skew angle and +10° skew angle for both cutting depths.

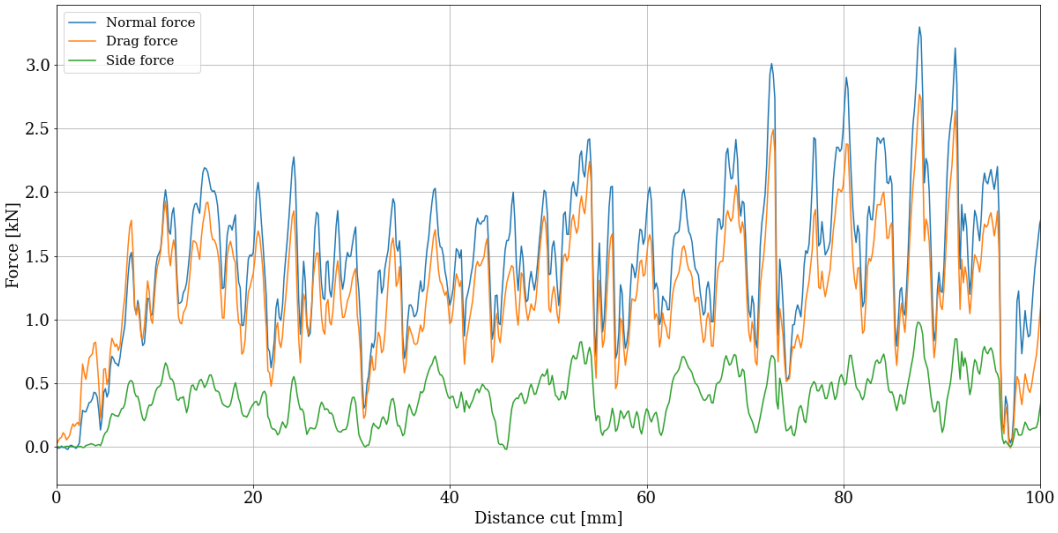

Figure 3.30: Cutting forces for 2 mm cutting depth, s/d = 3 and skew angle = 0°.

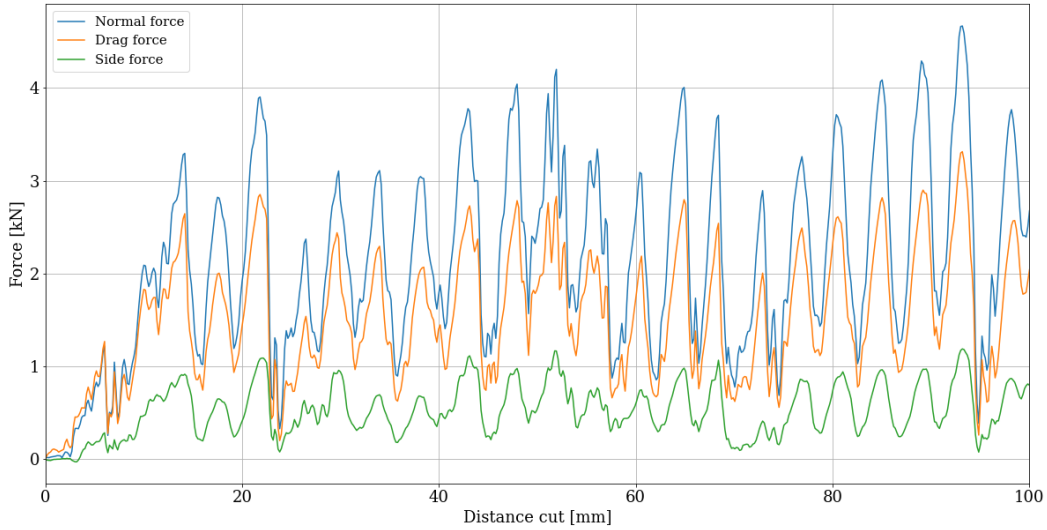

Figure 3.31: Cutting forces for 2 mm cutting depth, s/d = 3 and skew angle = −10°.

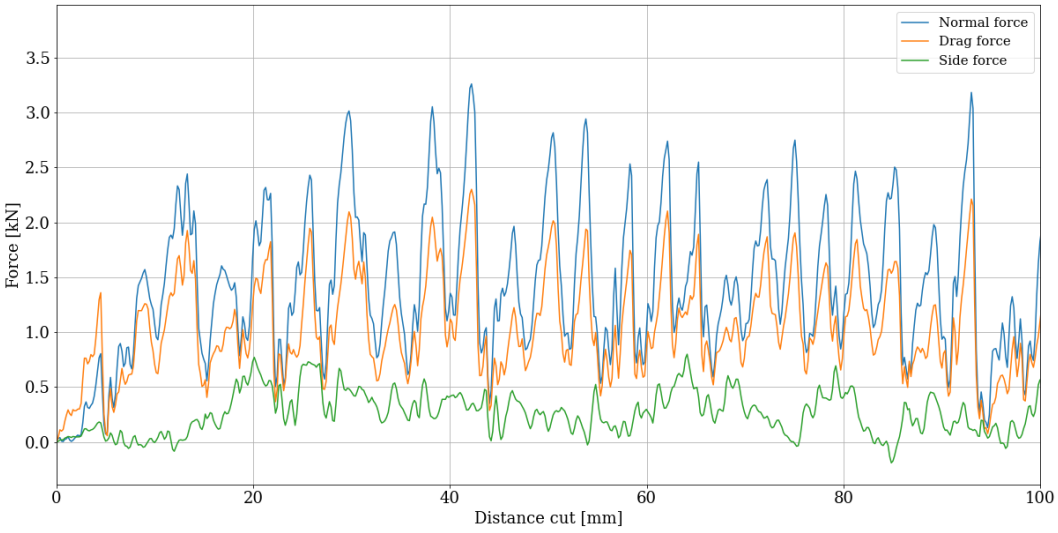

Figure 3.32: Cutting forces for 2 mm cutting depth, s/d = 3 and skew angle = +10°.

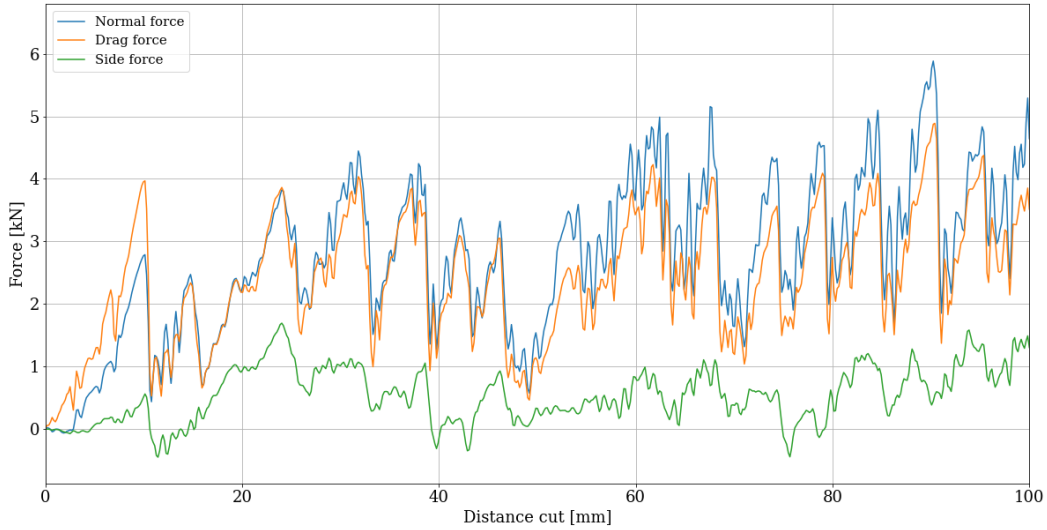

Figure 3.33: Cutting forces for 4 mm cutting depth, s/d = 3 and skew angle = 0°.

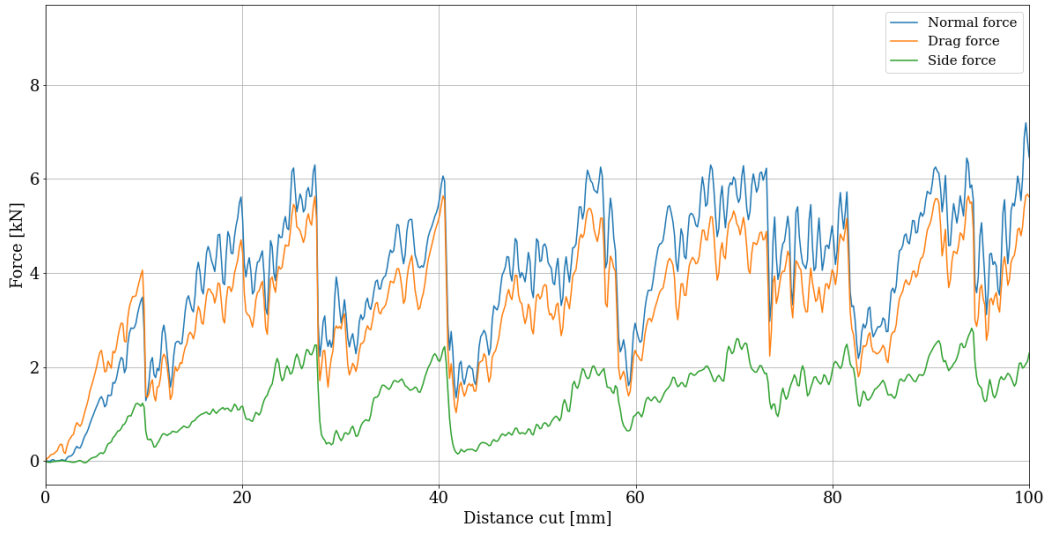

Figure 3.34: Cutting forces for 4 mm cutting depth, s/d = 3 and skew angle = $-10°$.

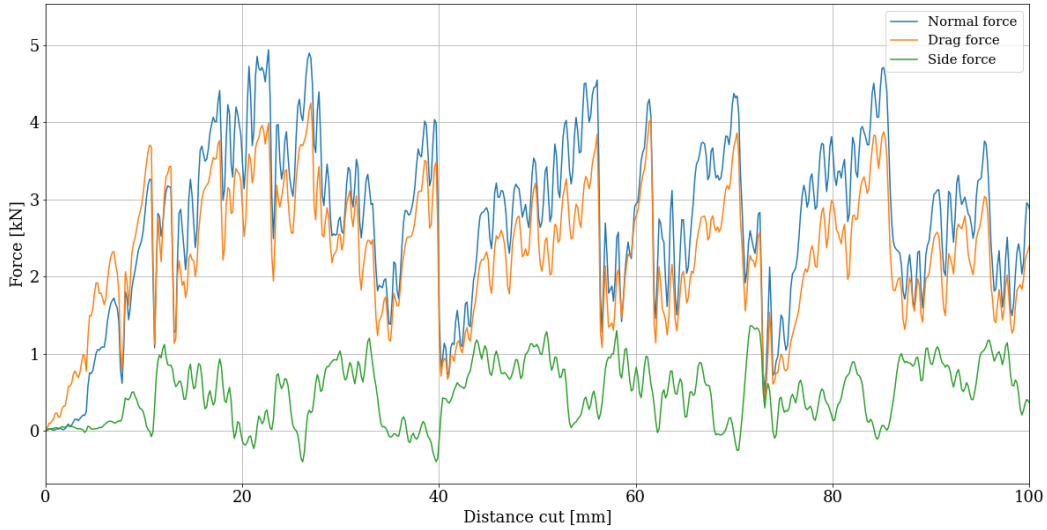

Figure 3.35: Cutting forces for 4 mm cutting depth, s/d = 3 and skew angle = $+10°$.

When comparing the cutting force signals for the 2 mm and 4 mm cutting depth the 4 mm cutting depth resembles a saw tooth shape where the 2 mm cutting depth resembles an impulsive signal. A fast Fourier transform (FFT) analysis was performed on the data to show the periodicity of the data. This is discussed in section 4.3.

For the 4 mm cutting depth, there is a larger increase in forces before a chip is formed. This can be seen when looking at the size of material that was collected after each cut. Figure 3.36a shows the chips for a cutting depth of 2 mm and figure 3.36b shows chips for a cutting depth of 4 mm.

(a) 2 mm cutting depth.

(b) 4 mm cutting depths.

Figure 3.36: Cut material of sandstone.

Figure 3.36 shows that at a cutting depth of 4 mm the chips that are formed are larger than the chips at a cutting depth of 2 mm. This is consistent with the behaviour observed from the cutting force signals.

Figure 3.37 shows the specific energy for the different cutting parameters.

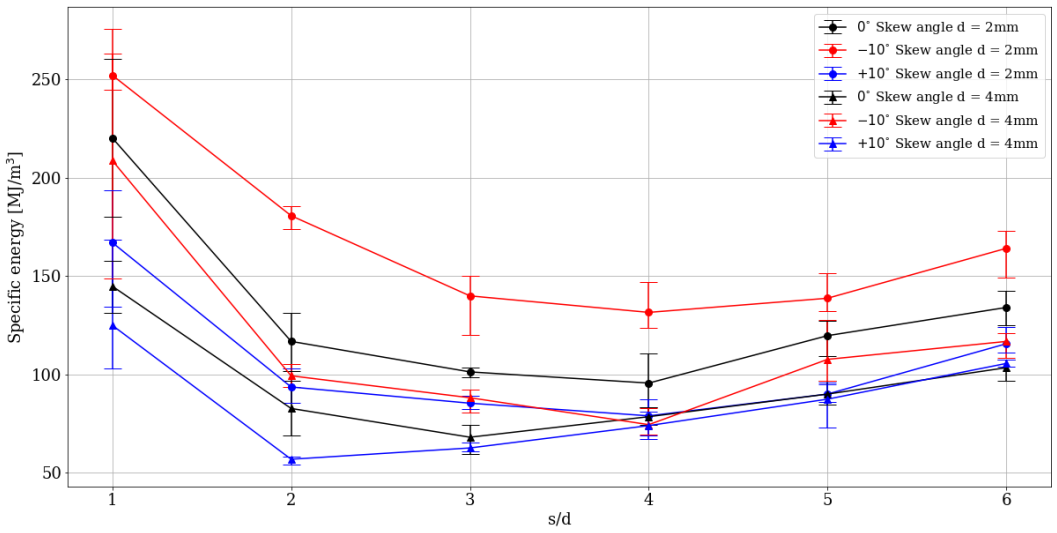

Figure 3.37: Specific energy for different cutting parameters.

The specific energy for both cutting depths follow the same trend. For both cutting depths the specific energy, when the pick has a positive skew angle, is lower than the zero skew angle and the negative skew angle. Also the specific energy, when the pick has a negative skew angle, is higher than both zero skew angle and positive skew angle. This applies for all values of s/d.

For positive skew angle of 10° the optimal s/d is 2, but this will cause side forces. For zero skew angle the optimal s/d is between 3 and 4. For negative skew angle of 10° the optimal s/d is 4. Thus

the skew angle has an influence on both the magnitude of the specific energy and the optimal s/d.

The results obtained for cutting the sandstone are similar to the results obtained by Park (Park et al., 2018). Park did their study on different types of cement mortar samples. The trends and range of magnitude of the forces and specific energy in this study are similar to that of Park.

This section shows that the LCM used in this study works as expected and can be used to obtain useful data about cutting UG2 reef samples.